

**GREEN SYNTHESIS AND CHARACTERIZATION OF
NICKEL OXIDE NANOPARTICLES USING AQUEOUS BARK
EXTRACT OF *Muntingia calabura* (MALAYAN CHERRY)**

By

KOH WEI FANG

A project report submitted to the Department of Chemical Science

Faculty of Science

Universiti Tunku Abdul Rahman

in partial fulfillment of the requirements for the degree of

Bachelor of Science (Honours) Chemistry

SEPTEMBER 2024

ABSTRACT

GREEN SYNTHESIS AND CHARACTERIZATION OF NICKEL OXIDE NANOPARTICLES USING AQUEOUS BARK EXTRACT OF *Muntingia calabura* (MALAYAN CHERRY)

KOH WEI FANG

Nickel oxide nanoparticles (NiO NPs) were synthesized through a green synthesis pathway utilizing the aqueous bark extract of *M. calabura* with nickel(II) acetate tetrahydrate (Ni-A) and nickel(II) nitrate hexahydrate (Ni-N) serving as precursor salts. The presence of different anions in various nickel salts significantly impacts the nucleation and growth of NiO NPs by establishing unique formation environments which consequently modify the arrangement and surface characteristics of the faceted planes. The synthesized NiO NPs were characterized using Fourier Transform Infrared Spectroscopy (FTIR), Ultraviolet-Visible (UV-Vis) Spectroscopy, X-ray Diffraction (XRD), Field Emission Scanning Electron Microscopy (FESEM), and Energy Dispersive X-Ray Spectroscopy (EDX). In this study, NiO NPs were successfully synthesized using two different precursor salts, nickel(II) acetate tetrahydrate (Ni-A) and nickel(II) nitrate hexahydrate (Ni-N). The NiO NPs synthesized from Ni-A exhibited a maximum absorption peak at 346 nm with a corresponding band gap

energy of 3.58 eV. FTIR analysis revealed a significant band at 479 cm^{-1} , attributed to NiO stretching vibrations that confirm the formation of NiO NPs. These NPs were spherical with particle sizes ranging from 44.7 - 65.6 nm, and displayed a trigonal (hexagonal axes) crystal structure with an average crystallite size of 18.53 nm. Similarly, the NiO NPs synthesized using Ni-N as the precursor salt showed a maximum absorption peak at 340 nm with a band gap energy of 3.64 eV. FTIR analysis indicated a band at 460 cm^{-1} corresponding to NiO stretching vibrations which further validated the synthesis of NiO NPs. The resulting NiO NPs were also spherical with particle sizes ranging from 37.8 - 61.6 nm, and exhibited a cubic crystal structure with an average crystallite size of 27.22 nm. According to the EDX analysis, both NiO NPs synthesized utilizing Ni-A and Ni-N as precursor salts were free of contaminants and consisted solely of nickel and oxygen elements. These findings highlight the morphology and optical characteristics of NiO NPs will be modified depending on the precursor salt used.

ABSTRAK

SINTESIS HIJAU DAN PENCIRIAN NANOPARTIKEL NIKEL OKSIDA DENGAN MENGGUNAKAN EKSTRAK AQUEOUS KULIT KAYU *Muntingia calabura* (KERUKUP SIAM)

Nanopartikel nikel oksida (NiO NPs) telah disintesis melalui sintesis hijau menggunakan ekstrak kulit kayu *M. calabura* dalam bentuk cecair bersama nikel(II) asetat tetrahidrat (Ni-A) dan nikel(II) nitrat heksahidrat (Ni-N) sebagai garam prekursor. Kehadiran anion yang berbeza dalam pelbagai garam nikel telah mempengaruhi nukleasi dan pertumbuhan NiO NPs dengan mewujudkan persekitaran pembentukan yang unik. Secara tidak langsung, situasi ini telah mengubah susunan, bentuk dan geometri serta ciri-ciri permukaan. NiO NPs yang disintesis telah dicirikan menggunakan Spektroskopi Inframerah Fourier Transform (FTIR), Spektroskopi Ultralembayung-nampak (UV-Vis), Difraksi X-ray (XRD), Mikroskop Elektron Pengimbasan Pelepasan Medan (FESEM), dan Spektroskopi Penyebaran Tenaga Sinar-X (EDX). Dalam kajian ini, NiO NPs berjaya disintesis menggunakan dua garam prekursor yang berbeza iaitu nikel(II) asetat tetrahidrat (Ni-A) dan nikel(II) nitrat heksahidrat (Ni-N). NiO NPs yang disintesis daripada Ni-A menunjukkan puncak penyerapan maksimum pada 346 nm dengan tenaga jurang jalur 3.58 eV. Analisis FTIR menunjukkan jalur yang signifikan pada 479 cm^{-1} yang dikaitkan dengan regangan NiO yang mengesahkan pembentukan NiO NPs. NiO NPs terhasil adalah berbentuk sfera dengan saiz zarah antara 44.7 - 65.6 nm, dan memaparkan struktur kristal

trigonal (paksi heksagonal) dengan saiz kristalit purata 18.53 nm. Begitu juga, NiO NPs yang disintesis menggunakan Ni-N sebagai garam prekursor menunjukkan puncak penyerapan maksimum pada 340 nm dengan tenaga jurang jalur sebanyak 3.64 eV. Analisis FTIR menunjukkan jalur pada 460 cm^{-1} yang berkaitan dengan regangan NiO yang lebih mengesahkan sintesis NiO NPs. NiO NPs yang terhasil juga berbentuk sfera dengan saiz zarah antara 37.8 - 61.6 nm, dan memaparkan struktur kristal kubik dengan saiz kristalit purata 27.22 nm. Menurut analisis EDX, kedua-dua NiO NPs yang disintesis menggunakan Ni-A dan Ni-N sebagai garam prekursor bebas daripada pencemaran dan terdiri hanya daripada unsur nikel dan oksigen. Penemuan ini menyoroti bahawa morfologi dan ciri optikal NiO NPs akan diubah bergantung kepada garam prekursor yang digunakan.

ACKNOWLEDGEMENT

I would like to express my heartfelt gratitude to everyone who supported me throughout this final year project. First and foremost, I am deeply grateful to my supervisor, Dr. Yip Foo Win, for his invaluable guidance, encouragement, and advice throughout the entire project. He consistently ensured that I stayed on the right track, and without his support, this project would not have progressed as smoothly.

I would also like to thank UTAR for providing the facilities and instruments that were essential for my research. Additionally, I am thankful to all the UTAR laboratory staff and officers of the Faculty of Science, especially Mr. Seou Chi Kien, for his guidance and assistance in operating specific instruments.

I extend my deep gratitude to all the lecturers who provided invaluable knowledge and guidance throughout my studies at UTAR, which enabled me to successfully undertake this project. Finally, I am profoundly thankful to my family and friends for their unwavering support and understanding throughout my academic journey at UTAR. Their encouragement and trust were vital to my success, supporting me to reach this milestone. Thank you!

DECLARATION

I hereby declare that this final year project report is based on my original work except for quotations and citations which have been duly acknowledged. I also declare that it has not been previously or concurrently submitted for any other degree at UTAR or other institutions.



KOH WEI FANG

APPROVAL SHEET

This final year project report entitled “**GREEN SYNTHESIS AND CHARACTERIZATION OF NICKEL OXIDE NANOPARTICLES USING AQUEOUS BARK EXTRACT OF *Muntingia calabura* (MALAYAN CHERRY)**” was prepared by KOH WEI FANG and submitted as partial fulfilment of the requirements for the degree of Bachelor of Science (Hons) Chemistry at Universiti Tunku Abdul Rahman.

Approved by:

____*Yip Foo Win*____

(Dr. Yip Foo Win)

Date: 13/09/2024

Supervisor

Department of Chemical Science

Faculty of Science

Universiti Tunku Abdul Rahman

FACULTY OF SCIENCE

UNIVERSITI TUNKU ABDUL RAHMAN

Date: 12 SEPTEMBER 2024

PERMISSION SHEET

It is hereby certified that KOH WEI FANG (ID No: 22ADB00462) has completed this final year project thesis entitled “GREEN SYNTHESIS AND CHARACTERIZATION OF NICKEL OXIDE NANOPARTICLES USING AQUEOUS BARK EXTRACT OF *Muntingia calabura* (MALAYAN CHERRY)” under the supervision of Dr. YIP FOO WIN from the Department of Chemical Science, Faculty of Science.

I hereby give permission to the University to upload the softcopy of my final year project thesis in pdf format into the UTAR Institutional Repository, which may be made accessible to the UTAR community and public.

Yours truly,



KOH WEI FANG

TABLE OF CONTENTS

	Page
ABSTRACT	ii
ACKNOWLEDGEMENTS	vi
DECLARATION	vii
APPROVAL SHEET	viii
PERMISSION SHEET	ix
TABLE OF CONTENTS	x
LIST OF TABLES	xiii
LIST OF FIGURES	xiv
LIST OF ABBREVIATIONS	xvii
CHAPTER	
1 INTRODUCTION	
1.1 Background of study	1
1.2 Nanoparticles (NPs)	3
1.2.1 Method of synthesizing nanoparticles	8
1.2.2 Application of nanoparticles	10
1.3 Nickel oxide nanoparticles (NiO NPs)	13
1.4 Green chemistry	15
1.5 <i>Muntingia calabura</i> (Malayan Cherry)	17
1.6 Objectives	20
2 LITERATURE REVIEW	
2.1 Green synthesis of nickel oxide nanoparticles	21
2.2 Phytochemicals compositions in <i>Muntingia calabura</i>	24
2.3 Green synthesis of NiO NPs using plant extract	26
2.3.1 Green synthesis and characterization of NiO NPs	26

	using soursop (<i>Annona muricata</i> L.) fruit peel extract	
	2.3.2 Green synthesis and characterization of NiO NPs	29
	using <i>Euphorbia heterophylla</i> L. leaves extract	
	2.3.3 Green synthesis and characterization of NiO NPs	33
	using <i>Averrhoa bilimbi</i> fruit peel extract	
	2.3.4 Green synthesis and characterization of NiO NPs	36
	using <i>Limonia acidissima</i> citrus fruit juice extract	
	2.4 Concluding remarks	40
3	MATERIALS AND APPARATUS	
	3.1 Materials	43
	3.2 Equipment	44
	3.3 Instrument	46
	3.4 Overview of research methodology	47
	3.5 Experimental procedure	48
	3.5.1 Collection and preparation of plant extracts	48
	3.5.2 Green synthesis of nickel oxide nanoparticles	49
	3.6 Percentage yield of synthesized nickel oxide nanoparticles	51
	(NiO NPs)	51
	3.7 Characterization of synthesized NiO NPs	52
	3.7.1 Fourier-Transform Infrared Spectroscopy (FTIR)	53
	3.7.2 Ultraviolet-Visible Spectroscopy (UV-Vis)	54
	3.7.3 Field Emission Scanning Electron Microscopy	
	(FESEM) and Energy Dispersive X-ray Spectroscopy	55
	(EDX)	
	3.7.4 X-ray Diffraction (XRD)	
4	RESULTS AND DISCUSSION	
	4.1 Green synthesis of NiO nanoparticles	57
	4.2 Percentage yield of synthesized nickel oxide nanoparticles	61
	(NiO NPs)	62
	4.3 Characterization of synthesized NiO NPs	62

4.3.1	Fourier Transform Infrared Spectroscopy (FTIR)	70
4.3.2	Ultraviolet-Visible Spectroscopy (UV-Vis)	74
4.3.3	Field Emission Scanning Electron Microscopy (FESEM)	77 80
4.3.4	Energy Dispersive X-ray Spectroscopy (EDX)	
4.3.5	X-ray Diffraction (XRD)	
5	CONCLUSION	
5.1	Conclusion	86
5.2	Future studies	87
	REFERENCES	88
	APPENDICES	97

LIST OF TABLES

Table		Page
1.1	Classification of nanoparticles based on structural composition	4
1.2	Applications of nanoparticles across various fields	11
1.3	Traditional uses of various parts of <i>M. calabura</i>	19
2.1	Summary of phytochemical screening in the aqueous extract of <i>M.calabura</i>	24
2.2	Summary of the different precursor salts and plant parts utilized in the synthesis of NiO NPs with their characterizations	41
3.1	List of equipment utilized with their functions	44
3.2	List of instruments employed with their functions	46
4.1	Percentage yield of synthesized NiO NPs from two precursor salts	61
4.2	Summary of FTIR spectra of bark extract of <i>M. calabura</i> , Ni-A, NiO NPs (Ni-A), Ni-N, and NiO NPs (Ni-N)	68
4.3	EDX analysis of weight percent with its atomic percent of the elements present in NiO NPs using Ni-A and Ni-N as precursor salts	79
4.4	Crystallite size calculated using the Debye-Scherrer's equation using Ni-A and Ni-N as precursor salts	85

LIST OF FIGURES

Figure		Page
1.1	Overview of nanomaterial classifications	4
1.2	Methods of synthesizing nanoparticles via bottom-up and top-down approaches	10
1.3	Cubic arrangement of NiO NPs	14
1.4	Rhombohedral arrangement of NiO NPs	15
1.5	12 Principles of green chemistry	16
1.6	Various parts of <i>Muntingia calabura</i> (a) leaves (b) fruits (c) flower	18
2.1	Plant parts utilized in the synthesis of Ni and NiO NPs	21
2.2	Covalent bonding between NPs and encapsulating compound	22
2.3	Bio-assisted reduction, surface capping, and stabilization of NiO nanoparticles	23
2.4	Appearance of <i>Annona muricata</i> L.	26
2.5	Schematic representation of the green synthesis of NiO NPs utilizing fruit peel extract from <i>A. muricata</i>	27
2.6	(a-b) TEM images, and (c) Particle size distribution histogram of NiO NPs	28
2.7	SEM image of NiO NPs	29
2.8	Appearance of <i>Euphorbia heterophylla</i> L.	30
2.9	XRD pattern of NiO NPs	31
2.10	(a) SEM image, (b) TEM image, and (c) EDX analysis of NiO NPs	32
2.11	FTIR spectrum of NiO NPs	33
2.12	Overview of the production of NiO NPs utilized fruit peels of <i>Averrhoa bilimbi</i>	34
2.13	(a) UV- Vis spectrum, and (b) Tauc plot of NiO NPs	35
2.14	(a-b) SEM images, (c) Particle size distribution histogram, and (d) EDX analysis of NiO NPs	36
2.15	(a) UV- Vis spectrum, and (b) Tauc plot of NiO NPs	37
2.16	XRD pattern of NiO NPs	38

2.17	(a) SEM image, (b) TEM image, and (c) EDX analysis of NiO NPs	39
2.18	FTIR spectrum of NiO NPs	40
3.1	Overview of the methodology	47
3.2	Flowchart for processing <i>M. calabura</i> bark into a powdered form	49
3.3	Extraction workflow diagram for <i>M. calabura</i> bark	49
3.4	Overview of the NiO NPs synthesis process	50
3.5	Perkin Elmer Spectrum Two model of FTIR analysis	52
3.6	Thermo Fisher Scientific Genesys 180 model of UV-Vis analysis	53
3.7	JSM-6701F and Oxford Instruments X-Max 50mm ² models of SEM-EDX analysis	55
3.8	Shimadzu XRD 6000 model for XRD analysis	56
4.1	Mechanism of synthesizing NiO NPs via a green synthesis pathway	60
4.2	FTIR spectra of (a) bark extract of <i>M. calabura</i> (b) NiO NPs using Ni-A as precursor salt	63
4.3	FTIR spectrum of Ni-A	63
4.4	Structures of compounds that contribute both O-H stretching and C=O stretching	65
4.5	FTIR spectra of (a) bark extract of <i>M. calabura</i> (b) NiO NPs using Ni-N as precursor salt	66
4.6	FTIR spectrum of Ni-N	67
4.7	Absorption spectrum of synthesized NiO NPs from Ni-A range from 200 nm to 1000 nm	70
4.8	Absorption spectrum of synthesized NiO NPs from Ni-N range from 200 nm to 1000 nm	71
4.9	Quantum confinement effects experienced by semiconductor nanoparticles as size decreases	73
4.10	FESEM images of NiO NPS synthesized by Ni-A as precursor salt at magnifications of (a) 10000× (b) 30000×	75
4.11	FESEM images of NiO NPS synthesized by Ni-N as precursor salt at magnifications of (a) 10000× (b) 30000×	76
4.12	EDX spectrum of the synthesized NiO NPs using Ni-A as precursor salt	78

4.13	EDX spectrum of the synthesized NiO NPs using Ni-N as precursor salt	78
4.14	XRD diffractogram of the synthesized NiO NPs using Ni-A as precursor salt	81
4.15	XRD diffractogram of the synthesized NiO NPs using Ni-N as precursor salt	82

LIST OF SYMBOLS/ABBREVIATIONS

\AA	Angstrom
<i>A. muricata</i>	<i>Annona muricata</i>
Ag	Silver
APS	American Physical Society
AR	Analytical research
Au	Gold
c	Speed of light
C=O	Carbonyl group
CAS	Chemical Abstracts Service
CdS	Cadmium sulfide
CdTe	Cadmium telluride
CH_3COO^-	Acetate ion
cm	Centimeter
cm^{-1}	Wavenumber or frequency unit
COO^-	Carboxylate ion
CP	Calcium phosphate
Cu	Copper

D	Crystallite size in diameter
<i>E. heterophylla</i>	<i>Euphorbia heterophylla</i>
EDX	Energy Dispersive X-ray
E_g	Band gap energy
eV	Electron volt
FESEM	Field Emission Scanning Electron Microscopy
FTIR	Fourier Transform Infrared
FWHM	Full width half maximum (FWHM) of the diffraction peak in radian 2θ
g	Gram
g/mol	Gram per mole
GaN	Gallium nitride
h	Planck's constant
HA	Hydroxyapatite
H-O-H	Water molecule
HOMO	Highest occupied molecular orbital
$h\nu$	Incident photon energy
ICDD	International Centre of Diffraction Standard
InAs	Indium arsenide

ISO	International Organisation for Standardisation
J	Joule
k	Scherrer's constant
K	Kelvin
KBr	Potassium bromide
LUMO	Lowest unoccupied molecular orbital
m	Meter
<i>M. calabura</i>	<i>Muntingia calabura</i>
mg	Milligram
mL	Millilitre
Ni	Nickel
Ni ²⁺	Nickel(II) ion
Ni ³⁺	Nickel(III) ion
Ni-A	Nickel(II) acetate tetrahydrate
Ni-N	Nickel(II) nitrate hexahydrate
NiO	Nickel oxide
NiO NPs	Nickel oxide nanoparticles
NLC	Nanostructured lipid carriers
NM	Nanomaterial

nm	Nanometer
NNI	National Nanotechnology Initiative
NO_3^-	Nitrate ion
NPs	Nanoparticles
O	Oxygen
O-H	Hydroxyl group
ROS	Reactive oxygen species
rpm	Revolutions per minute
SLN	Solid lipid nanoparticles
TEM	Transmission Electron Microscopy
Ti	Titanium
TiO_2	Titanium dioxide
UV-Vis	Ultraviolet-Visible
VB	Valence band
W	Watt
XRD	X-ray Diffraction
Zn	Zinc
ZnO	Zinc oxide
%	Percent

μ	Absorptivity coefficient
$^{\circ}$	Degree
$^{\circ}\text{C}$	Degree Celsius
λ_{max}	Maximum absorption wavelength
π	Pi

CHAPTER 1

INTRODUCTION

1.1 Background of study

Nanotechnology is widely recognized as an extremely promising field in the 21st century. The name 'nano' traces back to the Greek term for 'dwarf' and denotes something exceptionally small, precisely one-billionth of a meter (10^{-9} m). Nanotechnology is the capacity to examine, evaluate, manipulate, assemble, oversight, and produce materials on a nanometre size. The U.S. National Nanotechnology Initiative (NNI) interprets the meaning of nanotechnology as the application of science, engineering, and technology at the nanoscale, which ranges from 1-100 nm. At this scale, unique phenomena occur, allowing for innovative applications in domains such as chemistry, physics, biology, medicine, and electronics. Nanotechnology involves two key aspects. The first is scale, which it focuses on exploiting structures by regulating their form and dimension at the nanometre scale. The second aspect is novelty, where nanotechnology requires interacting with little objects in a way that makes use of some qualities inherent in the nanoscale (Bayda et al., 2019).

When Michael Faraday showed "gold colloid" samples to the Royal Society in 1857, it was the first instance of nanotechnology being demonstrated. He saw that the blue hue of a gold chloride solution changed to a ruby-red dispersion when he added phosphorus, but he didn't know why. Some reported different hues, such as ruby, green, violet, or blue, while others saw the dispersion of nanoscale gold particles becomes clear at certain wavelengths. Consequently, several theoretical investigations and experiments have been carried out to explain the distinctive characteristics of similar systems, now referred to as low-dimensional systems. Nearly a century later, Richard Feynman famously said, "There's Plenty of Room at the Bottom," during his talk at the American Physical Society (APS) assembly at Caltech in 1959, sparking interest in nanotechnology. (Bayda et al., 2019).

Globally, nanotechnology has completely transformed almost every industrial area, from large-scale production in sectors like environmental management, civil engineering, and automotive to small-scale manufacturing and processing in food, agriculture, and medicine. Researchers, entrepreneurs, scientists, technology professionals, environmentalists, and educators working together implies that the future of nano-based enterprises will continue to expand sustainably (Malik, Muhammad, and Waheed, 2023).

1.2 Nanoparticles (NPs)

Nanoparticles (NPs) are described by the International Organisation for Standardisation (ISO) as nano-sized substances possessing all external measurements within the nanometer scale, where the broadest and narrowest axes' length differences are minor. Terms like nanofibers or nanoplates are frequently used in place of nanoparticles when there is a considerable difference in size, usually greater than three times. NPs can vary in shape, size, and structure. Their dimensions usually span from 1-100 nm, and if they are smaller than 1 nm, they are called atom clusters. NPs can exist as single particles or as agglomerates, and they can be crystalline, with one or more crystals, or amorphous (Joudeh and Linke, 2022).

NPs can be categorized into five groups as illustrated in Figure 1.1 (Mekuye and Abera, 2023). As stated in Table 1.1, they are often divided into three divisions according to their composition: organic, inorganic, and carbon-based.

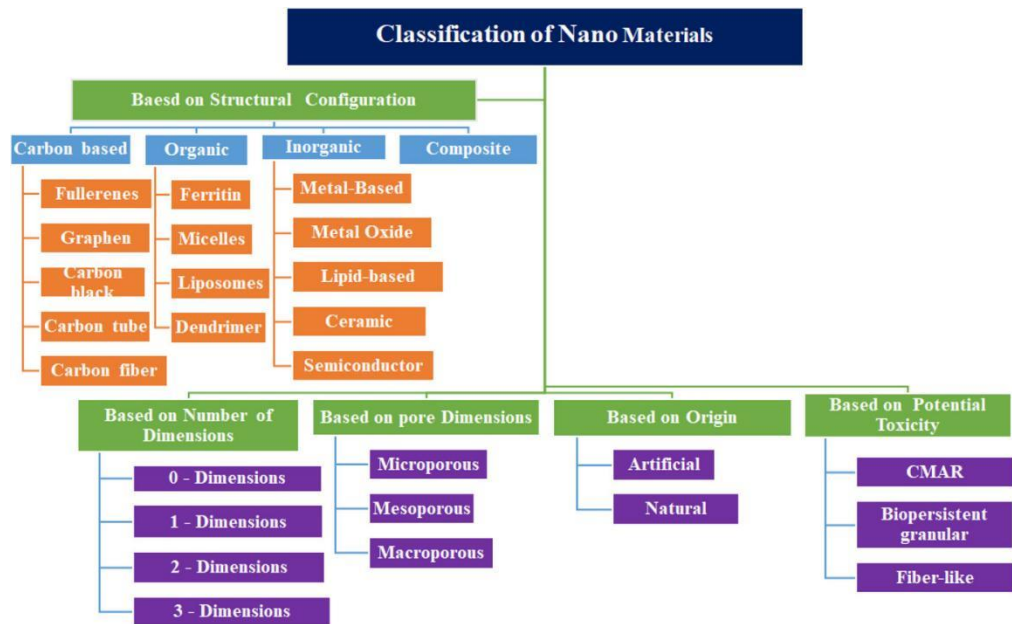


Figure 1.1: Overview of nanomaterial classifications (Mekuye and Abera, 2023)

Table 1.1: Classification of nanoparticles based on structural composition (Joudeh and Linke, 2022).

Types of nanoparticles	Descriptions
Organic	<ul style="list-style-type: none"> • Composed of polymers, lipids, proteins, carbohydrates, or other organic molecules • Properties: Non-toxic, biodegradable, sensitive to heat and light and labile • Examples: Dendrimers, liposomes, micelles, ferritin • Applications: Targeted drug delivery, cancer therapy

<p>Inorganic</p>	<ul style="list-style-type: none"> • Divided into groups that include metal-based, metal oxide-based, lipid-based, semiconductor, and ceramic <p><u>Metal-based</u></p> <ul style="list-style-type: none"> - Made of metal precursors - Properties: Unique optical, electrical, thermal, magnetic, and biological properties - Examples: Silver (Ag), gold (Au), copper (Cu), nickel (Ni), titanium (Ti), and zinc (Zn) (Yaqoob et al., 2020) - Applications: Nanodevices <p><u>Metal oxide-based</u></p> <ul style="list-style-type: none"> - Made of metal cations and oxide anions - Properties: Unique optical, electrical, thermal, magnetic, and biological properties - Examples: Titanium dioxide (TiO₂), zinc oxide (ZnO), nickel oxide (NiO) (Yaqoob et al., 2020) - Applications: Fluorescence and optical detectors, photovoltaic as well as medical (Alhalili, 2023)
------------------	---

Lipid-based

- Organic compounds that are reactive in colloidal form
- Properties: Great loading capacity, excellent thermal and temporal stability
- Examples: Solid lipid nanoparticles (SLN), nanostructured lipid carriers (NLC), and liposomes
- Applications: Cancer treatments
(García-Pinel et al., 2019)

Semiconductor

- Comprised of semiconductor components
- Properties: Unique characteristics between metals and non-metals, wide bandgaps, and notable changes in their properties due to bandgap adjustments
- Examples: Gallium nitride (GaN), Cadmium sulfide (CdS), Cadmium telluride (CdTe), Indium arsenide (InAs)
(Shah, Babar, and Ali, 2021)
- Applications: Electronic gadgets, optics, and photocatalysis

	<p><u>Ceramic</u></p> <ul style="list-style-type: none"> - Comprised of metal and metalloid oxides, carbonates, carbides, and phosphates. - Properties: High stability and high load capacity - Examples: Hydroxyapatite (HA), calcium phosphate (CP) (Lakshmi et al, 2017) - Applications: Biomedical applications, dye degradation, photonics, and optical electronics
Carbon-based	<ul style="list-style-type: none"> • Made of carbon atoms • Properties: Superior conduction capability, robustness, electron affinity, and distinct thermal, optical, and sorption features • Examples: Fullerenes, carbon black NPs, carbon quantum dots, nanodiamonds, carbon nano onions • Applications: Tissue engineering, delivery of drugs, storage of energy, photovoltaic gadgets, bioimaging, and environmental sensing

1.2.1 Methods of synthesizing nanoparticles

There are several methods for synthesizing NPs as two primary strategies are well recognized which are top-down and bottom-up. These methods vary regarding expense, speed, and effectiveness.

In top-down synthesis, bulk materials are fragmented into nano-sized particles. This may be accomplished by utilizing modern methods like lithography and precise engineering that created and refined by companies over the last few decades. Throughout the manufacturing process, precise engineering supports the majority of the microelectronics sector, and a combination of improvements may lead to excellent performance. The bottom-up method utilizes physical, chemical, and biological techniques to create nanostructures at the nanoscale (1-100 nm). This method uses a governed operation that causes the molecules and atoms to self-assemble. These materials can be employed straight in their mass, disorganized state, or as components to construct more intricate, ordered structures (Bayda et al., 2019). These two approaches are illustrated in Figure 1.2.

Physical techniques involve the utilization of physical factors like heat, electric discharge, plasma, or electromagnetic waves. These approaches are advantageous due to their speed and low chemical usage. However, physical synthesis procedures have limitations, including high energy requirements, broad particle size distribution, and low yield (Pryshchepa, Pomastowski, and

Buszewski, 2020). Chemical synthesis methods, also known as wet chemistry, are widely used due to their ability to produce high yields. However, these approaches often involve lengthy processing times, the application of dangerous substances, and a restricted number of metal combinations that can be utilized (Nyabadza et al., 2023).

Physical methods give poor yields, while chemical techniques have detrimental effects on the environment because they employ toxic solvents and produce dangerous byproducts that may regenerate (Ingle et al., 2023). Green synthesis has garnered significant focus lately in which the NPs are produced by extracting fungal, algal, bacterial, and plant extracts (mostly terrestrial). Various metabolites from these species serve as reducing agents throughout the NPs formation process (Chavali and Nikolova, 2019). The reducing agent reduces a precursor containing metallic ions by converting them into NPs. In biological synthesis approaches, a biological entity delivers the reducing agent. Consequently, biological synthesis approaches are subdivided into categories according to the organism that produces the reducing agent (Nyabadza et al., 2023).

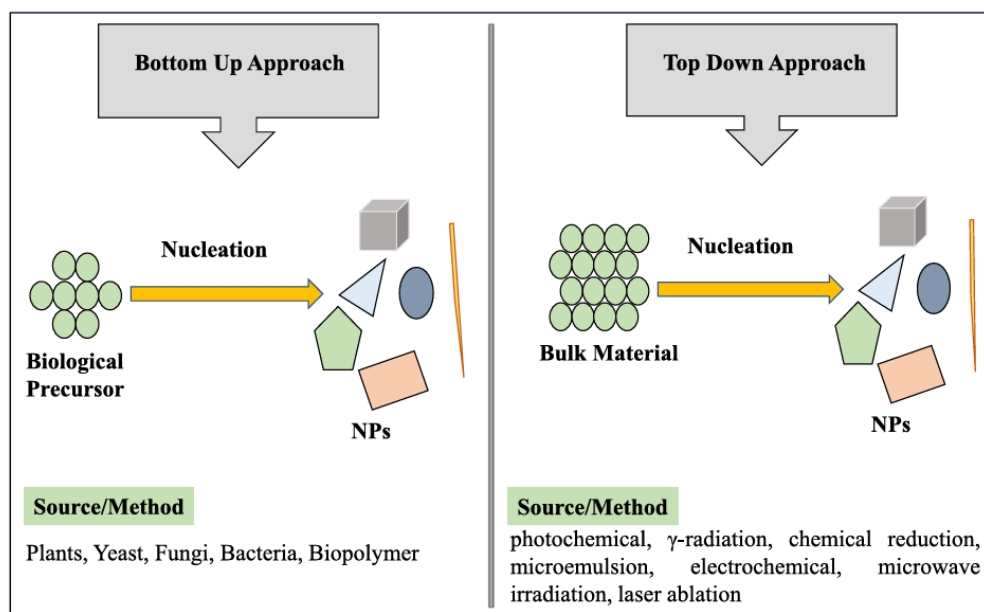


Figure 1.2: Methods of synthesizing nanoparticles via bottom-up and top-down approaches (Qamar and Ahmad, 2021).

1.2.2 Application of nanoparticles

NPs have been adopted in multiple sectors as a result of their nanometer-scale and unique properties. A brief outline of these applications can be found in Table 1.2 below.

Table 1.2: Applications of nanoparticles across various fields (Altammar, 2023).

Types of industry	Applications
Medicine	<ul style="list-style-type: none"> • Used as drug delivery <ul style="list-style-type: none"> - NPs transport medications to particular parts of the body • Used as imaging agents <ul style="list-style-type: none"> - NPs assist in the visualization of certain bodily locations • Used as antibacterial agents <ul style="list-style-type: none"> - NPs possess significant strong antibacterial properties.
Agriculture	<ul style="list-style-type: none"> • Used in pesticides and herbicides <ul style="list-style-type: none"> - NPs lower the need for chemicals and the risk of contaminating the environment. • Used in water purification <ul style="list-style-type: none"> - NPs cleanse drinking water, lowering the pollution of crops and increasing agricultural production.
Food	<ul style="list-style-type: none"> • Used in food fortification <ul style="list-style-type: none"> - NPs enhance the delivery of vital nutrients to food products more efficiently and effectively such as vitamins and minerals. • Used as sensor

	<ul style="list-style-type: none"> - NPs are utilized to boost both the specificity and sensitivity of food detectors, enabling them to identify a greater variety of substances or impulses.
Electronics and automotive	<ul style="list-style-type: none"> • Used in display technologies <ul style="list-style-type: none"> - NPs increase the brightness, colour, and contrast of the picture • Used in data storage <ul style="list-style-type: none"> - NPs possess the capability to store and retrieve data through magnetism
Defensive	<ul style="list-style-type: none"> • Used as protective coatings <ul style="list-style-type: none"> - NPs increase the coating's mechanical characteristics and endurance, increasing its resistance to damage and corrosion of defensive equipment.

1.3 Nickel oxide nanoparticles (NiO NPs)

Nickel oxide (NiO) is a transition metal oxide exhibiting a cubic arrangement (Ahmad et al., 2022). Ni cations usually display an octahedral arrangement with a valence state of $2+$ ($3d^8$) as NiO forms crystals in a rock-salt appearance as illustrated in Figure 1.3. NiO exhibits a cubic crystal form at the Néel temperature (523 K). As the temperature falls below the Néel threshold, the crystals adopt a rhombohedral form and appear a little deformed as shown in Figure 1.4, which corresponds to antiferromagnetic ordering (Diao et al., 2020). The Néel temperature is the critical temperature whereby the magnetization of an antiferromagnetic system undergoes a behaviour change. It is influenced by the Curie constant and the interactions of the magnetic field (Reis, 2013).

It has developed popularity considering its ability to be used across different applications including gas detectors, catalysis, electrochromic coatings, and magnetic substances. Additionally, it is extensively used in photocathodes that are dye-sensitized. It features anodic electrochromism, great endurance, and electrochemical robustness, a high spin optical density, and several production possibilities. NiO semiconductors are also becoming a popular focus in recent studies owing to their inexpensive cost that serves as an ion storage substance (El-Kemary, Nagy, and El-Mehasseb, 2013). It functions as a p-type semiconductor, whereby positive holes transport electrical current. (Ahmad et al., 2022). This occurs because Ni^{2+} ions are oxidized to Ni^{3+} ions. Moreover, some Ni^{2+} ions diffuse out to balance the charge, creating cation vacancies. The

material's conductivity is attributed to the electron transfer between Ni^{2+} and Ni^{3+} ions, allowing Ni^{3+} ions to move freely. Consequently, black NiO exhibits p-type semiconductor behavior (Azadeh, 2008). It is typically non-stoichiometric, with a minor presence of Ni^{3+} ions alongside Ni^{2+} ions within the crystal lattice (Ahmad et al., 2022). It is anticipated that NiO in the nanoscale would have superior characteristics than NiO NPs in the micrometer dimension owing to the volume impact, quantum size effect, and surface impact. In addition, it possesses a large band gap along with excellent chemical and thermal inertness (El-Kemary, Nagy, and El-Mehasseb, 2013). NiO NPs are being investigated considering their nano-scale dimensions resulting in distinct properties compared to most other NPs. The surface area to volume ratio variations and their electro-optical, magneto-optical, chemical, and mechanical characteristics result in unique optical, electronic, and physiochemical capabilities (Hong et al., 2021).

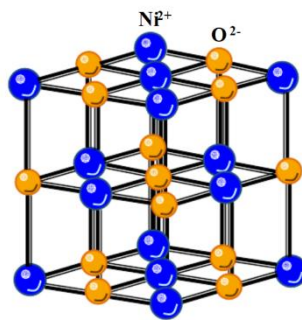


Figure 1.3: Cubic arrangement of NiO NPs (Diao et al., 2020).

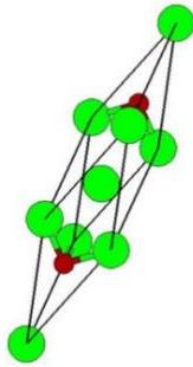


Figure 1.4: Rhombohedral arrangement of NiO NPs (Gandouzi et al., 2023).

1.4 Green chemistry

Green chemistry is an approach that uses innovative scientific methods to address environmental challenges. The aim is to develop chemical items and methods that minimize or completely avoid the use or production of hazardous materials. The Twelve Principles of Green Chemistry were suggested by Paul T. Anastas and John C. Warner in 1991 (Singh, 2023) as depicted in Figure 1.5.

The theory of "Green Chemistry" for "Sustainable Development" has garnered significant attention in the last ten years. Sustainable development is growth that satisfies present needs while also taking into account the ability of future generations to satiate their own needs. This concept is particularly crucial for various chemistry-related industries due to concerns about contamination and the overuse of natural assets. The three most crucial preconditions for the

formation of NPs are the choice of an environmentally benign solvent, a suitable benign reduction agent, and a harmless stabilizing substance. NPs can be formed via different methods, the most prevalent methods are physical, chemical, and biological methods. Chemical techniques are often expensive and utilize hazardous chemicals which contribute to a significant detrimental effect on the ecosystem. On the other hand, green synthesis offers a less dangerous, biocompatible, and more ecologically acceptable approach to producing nanoparticles for various applications including biomedicine. This green synthesis is achieved using fungi, algae, bacteria, and plants. Among these, various plant parts are frequently used to synthesize different types of NPs. Plant extracts enable the formation of NPs with specific dimensions, forms, and components. Furthermore, an extensive number of phytochemicals found in its extract function as naturally occurring reducers throughout the formation of NPs. Plant-derived NPs are also thought to be less likely to generate adverse reactions in individuals than those artificially produced NPs (Hano and Abbasi, 2021).



Figure 1.5: 12 Principles of green chemistry (Singh, 2023).

1.5 *Muntingia Calabura* (Malayan Cherry)

Plants with medicinal properties are essential for curing human illnesses. In poor nations, conventional treatment offers basic medical care to over 80% of the population and approximately 85% of these treatments originate from plant extracts. There is a significant need to explore the potential pharmacological benefits of various medicinal plants. *Muntingia calabura* L. (Elaeocarpaceae) is one such plant that has recently been recognized for its medicinal properties (Mahmood et al., 2014).

Muntingia calabura is referred to as "kerukup siam" in Malaysia, particularly by the Malay community, and is frequently recognized as the "Jamaican cherry" around the world. This species is the sole member of the genus *Muntingia* and is indigenous to the Greater Antilles, tropical regions of South and Central America, and others. The plant is widely grown in tropical regions of Southeast Asia, such as Malaysia. *M. calabura* is often used as a tree for planting at the side of the roads in Malaysia.

This tree exhibits fast growth and features thin branches that stretch out laterally, with a height ranging from 7.5-12.0 meters. The evergreen leaves of *M. calabura* are either lanceolate or oblong, and they range in length from 5.0-12.5 cm when grouped alternately. They are deep green with long-pointed at their tips and asymmetrical at the base. The leaves have fine hairs on the upper surface, while the underside is covered in grey or brown hairs and has irregular serrations. The flowers are 1.25-2.00 cm in diameter and appear singly or in pairs or trios within

the axils of the leaves. Each flower features five green sepals, five white petals, and numerous noticeable yellow stamens (Mahmood et al., 2014). The fruits are spherical, measuring about 1.5 cm in diameter, with a soft fragile outer skin and light-brown interior. They possess a sugary and fig-like flavour with small yellowish seeds inside (Shih, 2009). Figure 1.6 depicts the various parts of *M. calabura* and they are used traditionally to treat various illnesses as outlined in Table 1.3. Other than being in traditional treatment, the fruits can be consumed fresh and typically baked in tarts or prepared into jam (Zakaria et al., 2007).



(a) Leaves

(b) Fruits

(c) Flower

Figure 1.6: Various parts of *Muntingia calabura* (a) leaves (b) fruits (c) flower.

Table 1.3: Traditional uses of various parts of *M. calabura* (Kuchekar et al., 2021).

Parts of <i>M. calabura</i>	Traditional uses
Flowers	<ul style="list-style-type: none"> • Served as an infection control agent as well as for alleviating swelling in the lower limbs in Peru. • Used as a tranquilizer and tonic in Colombia • Treat headaches and incipient colds, and as antispasmodics and anti-dyspeptics in Philippines.
Leaves	Boiling or steeping in water is utilized to relieve stomach ulcers, enlargement of the prostate gland, headaches, and colds.
Roots	Employed to induce abortion in Malaysia and to stimulate menstrual flow in Vietnam.
Barks	Employed as a rinse to minimize oedema in the lower limbs (Zakaria et al., 2006).

1.6 Objectives

This study aimed to synthesize and characterize nickel oxide nanoparticles from plant extracts. The detailed objectives are outlined below:

1. To synthesize nickel oxide nanoparticles (NiO NPs) from the aqueous extract barks of *Muntingia calabura* through a green synthesis pathway using nickel(II) acetate tetrahydrate (Ni-A) and nickel(II) nitrate hexahydrate (Ni-N) as precursor salts.

2. To characterize nickel oxide nanoparticles (NiO NPs) using Fourier Transform Infrared Spectroscopy (FTIR), UV-Visible Spectroscopy (UV-Vis), X-ray Diffraction (XRD), Field Emission Scanning Electron Microscopy (FESEM) and Energy Dispersive X-ray Spectroscopy (EDX).

3. To study the characterization of NiO NPs synthesized using nickel(II) acetate tetrahydrate (Ni-A) and nickel(II) nitrate hexahydrate (Ni-N) as precursor salts.

CHAPTER 2

LITERATURE REVIEW

2.1 Green synthesis of nickel oxide nanoparticles

The biological method utilizing plant sources to synthesize NPs has been increasingly popular over the past 30 years owing to inexpensive and environmentally benign techniques being used (Kato and Suzuki, 2020). Figure 2.1 depicted the various parts of plants utilized in the production of NiO NPs.

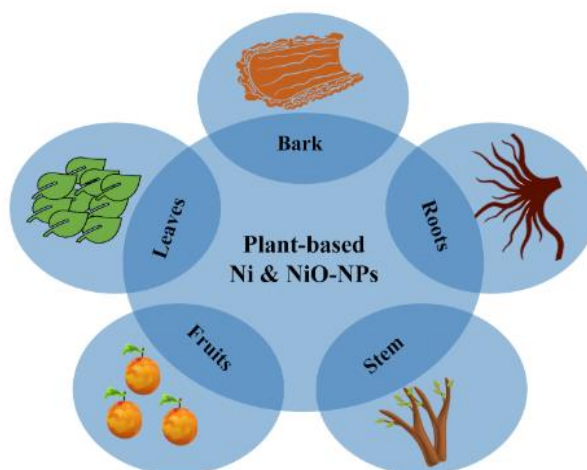


Figure 2.1: Plant parts utilized in the synthesis of Ni and NiO NPs (Maind et al., 2024).

The bioactive plant constituents that function as encapsulating and stabilizing substances including phenolic compounds, alkaloids, flavonoids, and polyphenols aid in the conversion of nickel salt to NiO NPs. The encapsulating compound consists of a hydrophilic head that reacts with the Ni²⁺ ions of NPs and the hydrophobic hydrocarbon chain reacts with the environment as illustrated in Figure 2.2. It is referred to as an amphiphilic molecule. Different approaches exist for both ends of encapsulating compounds to interact with their environment (Javed et al., 2020).

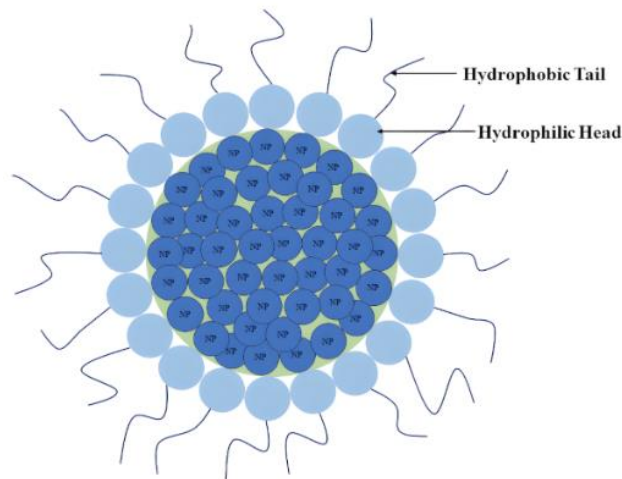


Figure 2.2: Covalent bonding between NPs and encapsulating compound (Maind et al., 2024).

One of the main restrictions on the creation of NPs is the development of clusters as well as aggregation. The aggregation of NPs affects the issues of unregulated development and robustness of colloids. The use of encapsulating and stabilizing chemicals is crucial in getting around this restriction. As seen in Figure 2.3, plant-derived compounds function as encapsulating and stabilizing compounds and stop nanoparticles from clumping or aggregating. The bioactive compounds

in plant extract are conducted via two mechanisms which are the development of metal ion-containing intermediates in different oxidation states and function as encapsulating substances for non-agglomerated NPs structures.

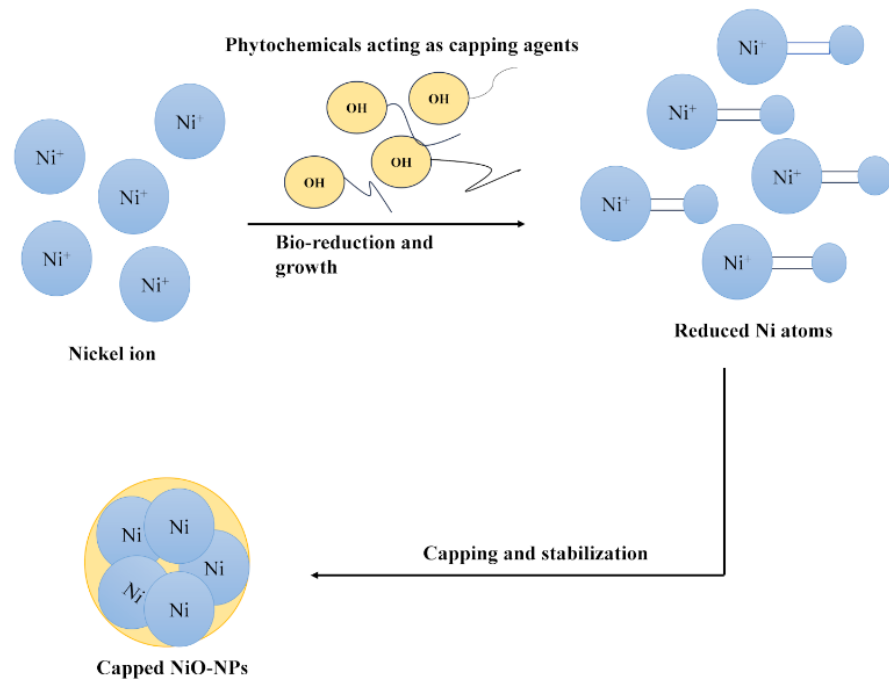


Figure 2.3: Bio-assisted reduction, surface capping, and stabilization of NiO nanoparticles (Maind et al., 2024).

2.2 Phytochemicals compositions in *Muntingia calabura*

Plants possess an infinite capacity to produce secondary metabolites. These compounds act as protective agents against predation by microorganisms, insects, and herbivores (Mallikharjuna et al., 2007). In addition, the compounds possess potential therapeutic properties for instance they reveal antimicrobial abilities, as a result of compounds synthesized during the plant's secondary metabolic pathway (Priya and Yasmin, 2022). According to a study conducted by Priya and Yasmin (2022), the phytochemical screening depicted that several bioactive compounds were present in the aqueous extract of *M.calabura* by carrying out various tests as tabulated in Table 2.1.

Table 2.1 : Summary of phytochemical screening in the aqueous extract of *M.calabura* (Priya and Yasmin, 2022).

Chemical compounds	Test/ Reagent	Observation	Result
Flavonoid	Ammonium test	A yellow colour solution was observed	(+)
Phenolics	Ferric chloride test	A dark green or bluish-black colour solution was observed	(+)

Saponins	Water	Foam was formed upon shaking the solution	(+)
Tannins	Braymer's test	No blue-green colour solution was observed	(-)
Terpenoids	$\text{CHCl}_3 + \text{H}_2\text{SO}_4$	No grey-coloured solution was formed	(-)
<p>(+) : Detected</p> <p>(-) : Not detected</p>			

2.3 Green synthesis of NiO NPs using plant extract

2.3.1 Green synthesis and characterization of NiO NPs using soursop

(Annona muricata L.) fruit peel extract.

The study conducted by Aminuzzaman et al. (2021) utilized the fruit peel of *A. muricata* to synthesize NiO NPs. It is a member of the Annonaceae family and the popular name is called soursop as depicted in Figure 2.4. Huge, dark green leaves cover this little, upright, perpetually green plant, which grows to a height of around 5-8 meters. The fruit of the tree is appetizing and grows to a huge, light green, oval or hearts-like fruit with white, fibrous flesh when completely mature. *A. muricata* has historically been used in medicine to cure a variety of ailments, notably joint pain, neuralgia, respiratory disorders, diarrhea, dysentery, a high fever, malaria, and malignancies, especially those of the liver and breast (Aminuzzaman et al., 2021). In this research, the precursor salt utilized is nickel acetate, and the procedure is summarized in Figure 2.5.



Figure 2.4: Appearance of *Annona muricata* L. (Quiroga Ledezma, 2020).

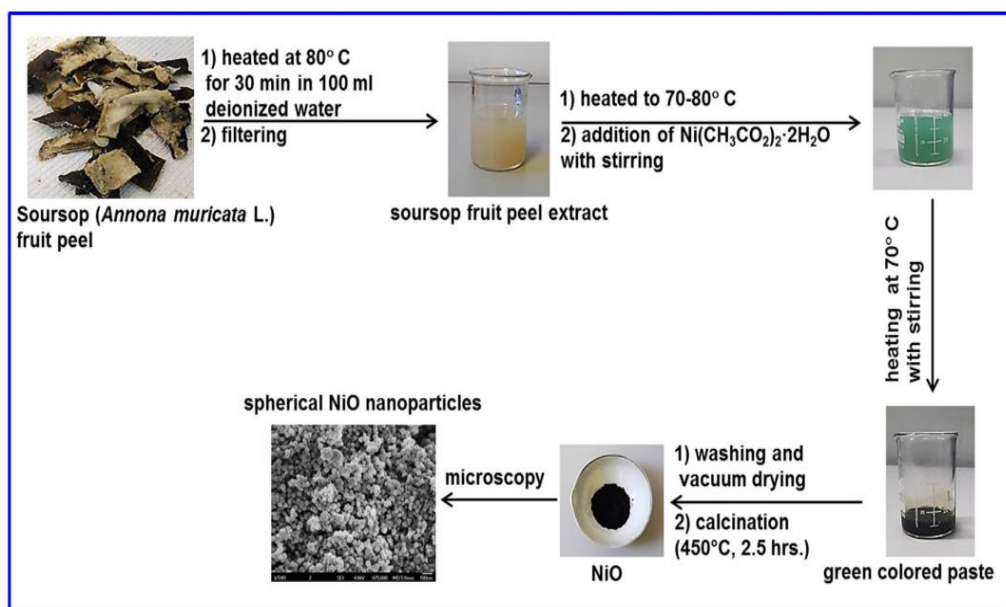


Figure 2.5: Schematic representation of the green synthesis of NiO NPs utilizing fruit peel extract from *A. muricata* (Aminuzzaman et al., 2021).

The XRD analysis shows that the synthesized NiO NPs exhibited the crystal system of cubic that matched with ICDD Card No. 01-071-6723. The diffraction peaks at 2θ were found at 37.24° , 43.32° , 62.80° , 75.64° , and 79.50° that matched the crystal structure planes of (111), (200), (220), (311), and (222) respectively. The strong and intense accurately suggested a high degree of crystalline structure. In addition, the NiO NPs were produced at optimal arrangement in the (200) direction, and the mean crystallite size obtained was 50.50 nm (Aminuzzaman et al., 2021).

According to Figure 2.6, TEM pictures demonstrated and validated the spherical form of the synthesized NiO NPs which vary in diameter from 20-90 nm and the typical dimension of 56 nm in conformity with the dimensions of the crystallite determined by the XRD analysis.

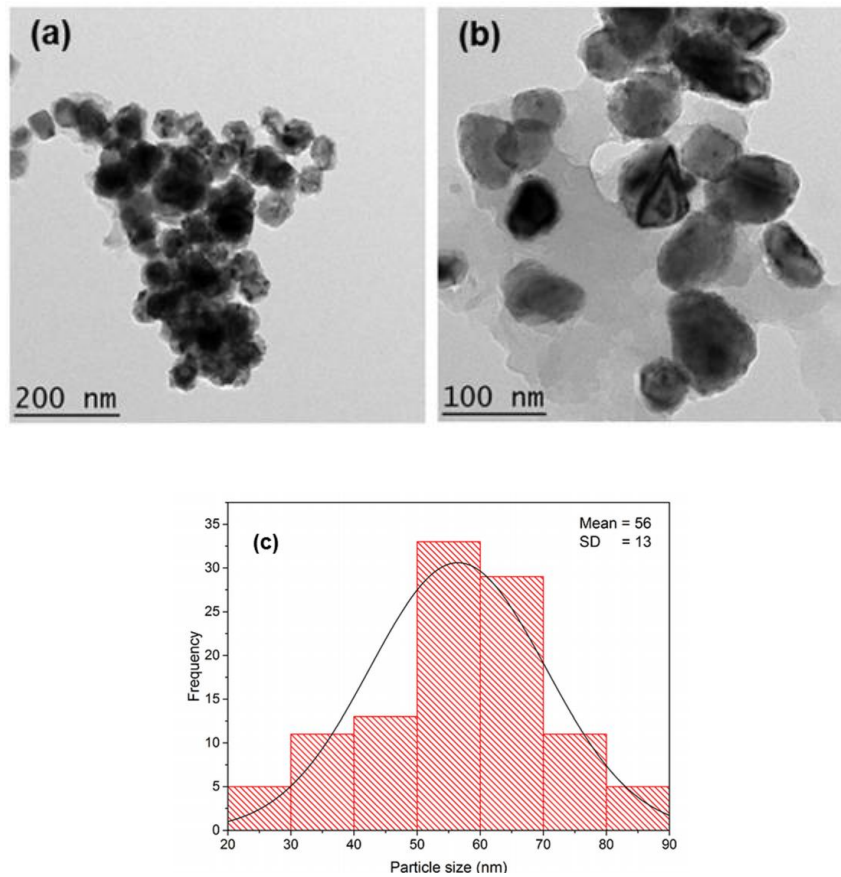


Figure 2.6: (a-b) TEM images, and (c) Particle size distribution histogram of NiO NPs (Aminuzzaman et al., 2021).

Based on Figure 2.7, FESEM pictures of NiO NPs also revealed that the particles are clumped together and have a spherical form which is consistent with TEM micrographs. It was determined that the interactions of magnetic forces between the particles were responsible for this particle aggregation (Aminuzzaman et al., 2021).

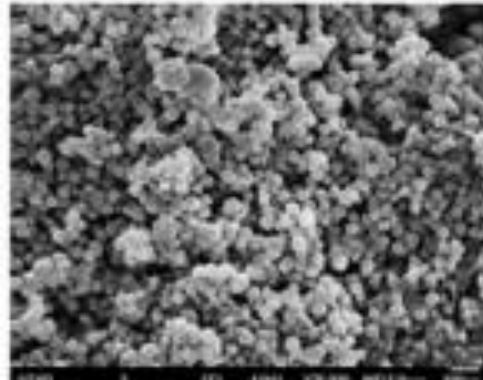


Figure 2.7: SEM image of NiO NPs (Aminuzzaman et al., 2021).

2.3.2 Green synthesis and characterization of NiO NPs using *Euphorbia heterophylla* L. leaves extract.

The leaves of *Euphorbia heterophylla* L. were utilized by Lingaraju et al. (2020) in the investigation of the production of NiO NPs. *E. heterophylla* as depicted in Figure 2.8 has a well-established medicinal benefit and its common name is wild poinsettia. It is a non-woody plant that can reach 200 cm tall, according to the circumstances (CABI, 2022). Additionally, it is a member of the

Euphorbiaceae family and it is primarily employed in treating a variety of illnesses. In this study, nickel nitrate hexahydrate was utilized as precursor salt and the calcination was carried out at 300°C for 3 hours (Lingaraju et al., 2020).



Figure 2.8: Appearance of *Euphorbia heterophylla* L. (CABI, 2022).

XRD diffractogram as illustrated in Figure 2.9 showed that NiO NPs exhibited Bunsenite lattice with mean crystallite sizes of 15 nm. The planes' respective maxima corresponded with (1 1 1), (2 0 0), (2 2 0), (3 1 1), and (2 2 2) which were all in good agreement with ICCD Card No. 04-0835 with mean crystallite size obtained was 15 nm.

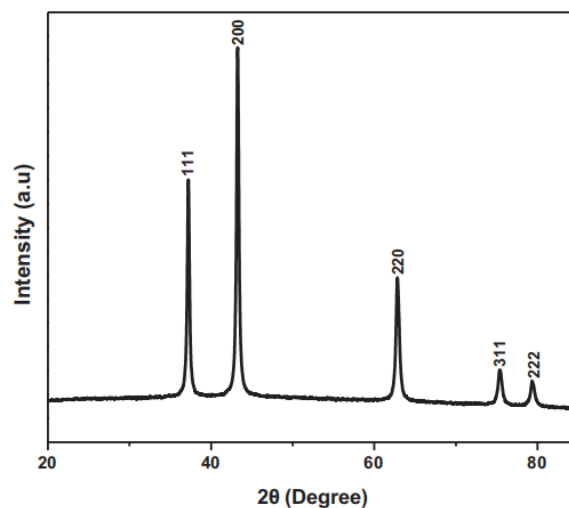


Figure 2.9: XRD pattern of NiO NPs (Lingaraju et al., 2020).

According to Figure 2.10 (a), rhombohedral forms of NiO NPs were obtained with aggregation occurring. The diameter of NPs ranged from 12-15 nm as depicted in Figure 2.10 (b) which were nearly identical to the XRD analysis of 15 nm attained. The atomic determination of NiO NPs was illustrated in Figure 2.10 (c) and showed no indications of contamination.

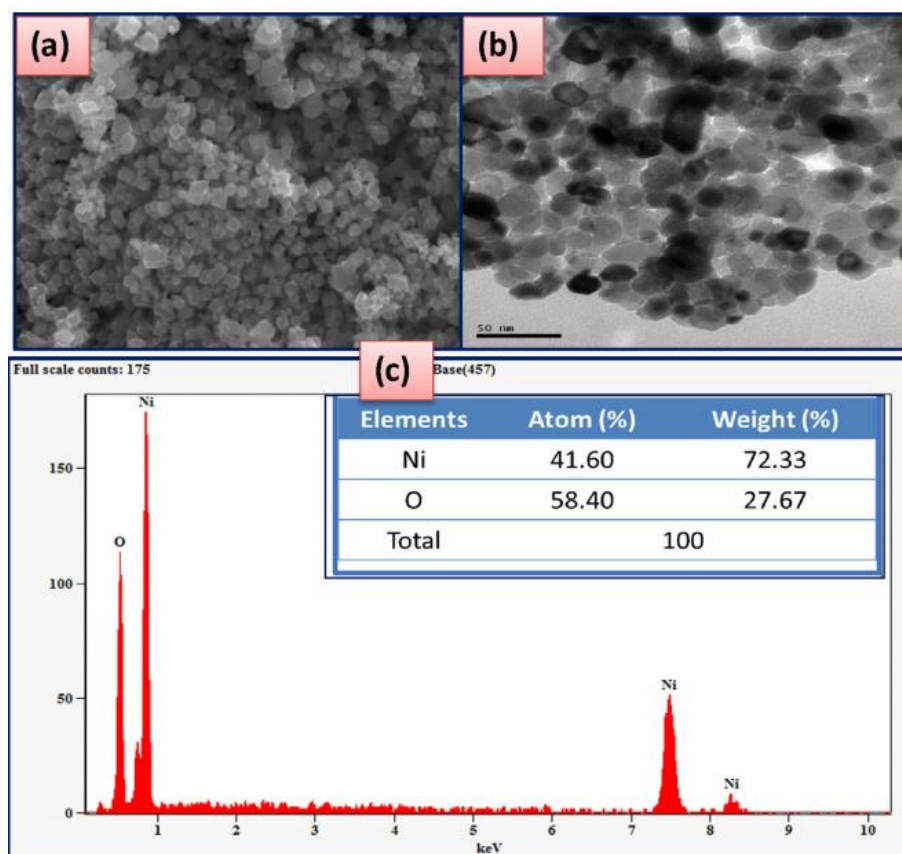


Figure 2.10: (a) SEM image, (b) TEM image, and (c) EDX analysis of NiO NPs (Lingaraju et al., 2020).

Based on the FTIR spectrum of NiO NPs depicted in Figure 2.11, a wide O-H stretching band was observed at 3441 cm^{-1} corresponding to phenol and carboxylic acid. Owing to the presence of water molecules a band located at 1631 cm^{-1} indicated bending H-O-H vibration. The distinct bands of the oxide groups are found at 1037 , 1112 , 1388 , and 1462 cm^{-1} accordingly. Lastly, the significant band that indicated the presence of NiO NPs was located at 452 cm^{-1} attributed to the vibrational mode of NiO.

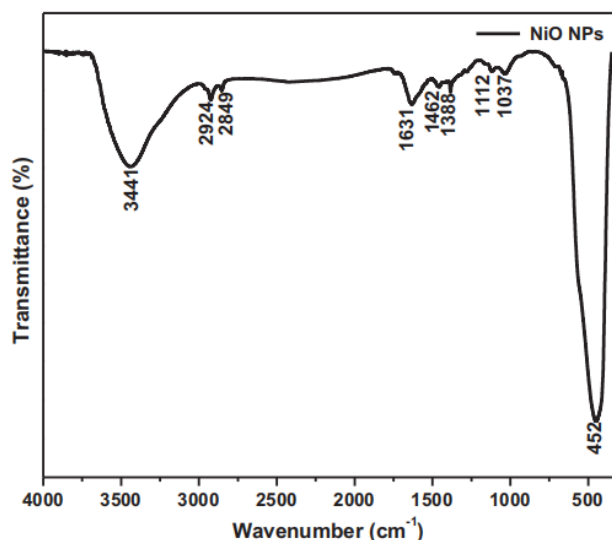


Figure 2.11: FTIR spectrum of NiO NPs (Lingaraju et al., 2020).

2.3.3 Green synthesis and characterization of NiO NPs using *Averrhoa bilimbi* fruit peel extract.

Averrhoa bilimbi, often known as "Bilimbi" as well as the "cucumber tree," is a multipurpose and everlasting rainforest flora that is a member of the Oxalidaceae family. This nutrient-dense and malty fruit that develops on the trunks of lofty trees is linked to the starfruit that is extensively grown across Asia. In addition, the fruit is rich in Vitamin C and treats numerous ailments including fever, coughing, and others (Haritha et al., 2022). The study by Haritha et al. (2022) employed *Averrhoa bilimbi* fruit peels for synthesizing NiO NPs using nickel nitrate hexahydrate as the precursor salt. The calcination temperature was 600°C for 4 hours in the muffle furnace. The overview of the production of NiO NPs is illustrated in Figure 2.12.

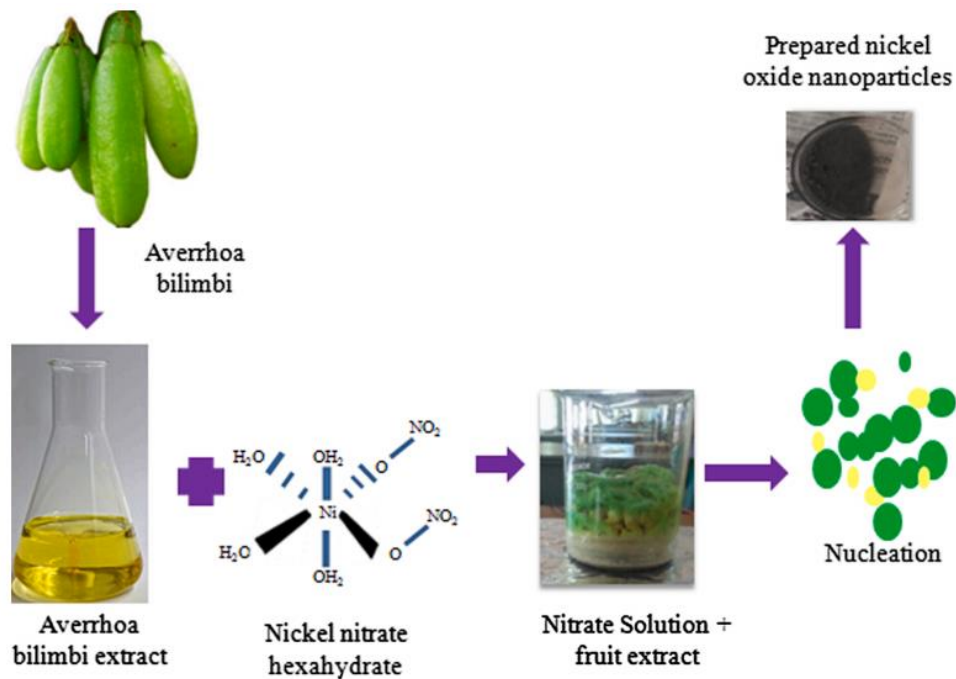


Figure 2.12: Overview of the production of NiO NPs utilized fruit peels of *Averrhoa bilimbi* (Haritha et al., 2022).

Based on Figure 2.13, NiO NPs had the maximum absorption peak at 340 nm owing to the charge transfer from ligand to metal, and the band gap energy determined using the Tauc plot was found to be 2.97 eV.

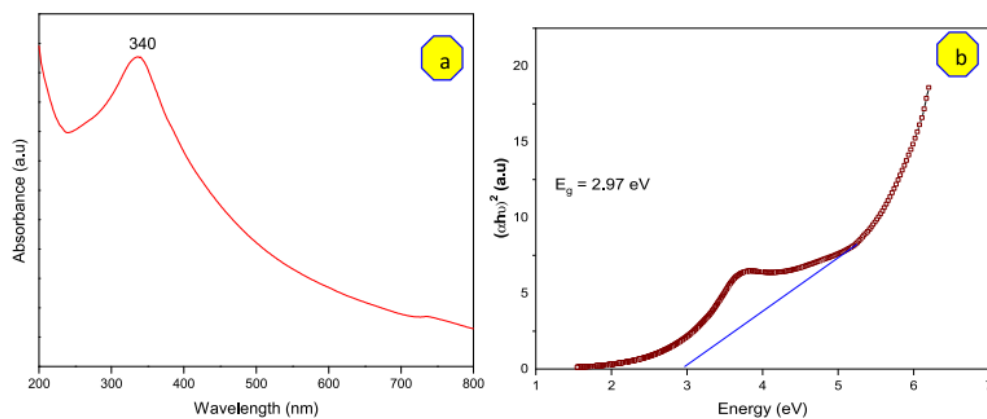


Figure 2.13: (a) UV- Vis spectrum, and (b) Tauc plot of NiO NPs (Haritha et al., 2022).

The SEM images in Figure 2.14 (a-b) showed that the spherical NiO NPs having a homogeneous size distribution and no aggregation were predicted. The NiO NPs obtained were within 110 to 120 nm as illustrated in Figure 2.14(c). Figure 2.14(d) showed the EDX determination conducted which indicated NiO NPs were made up entirely of Ni and O elements with no contaminants.

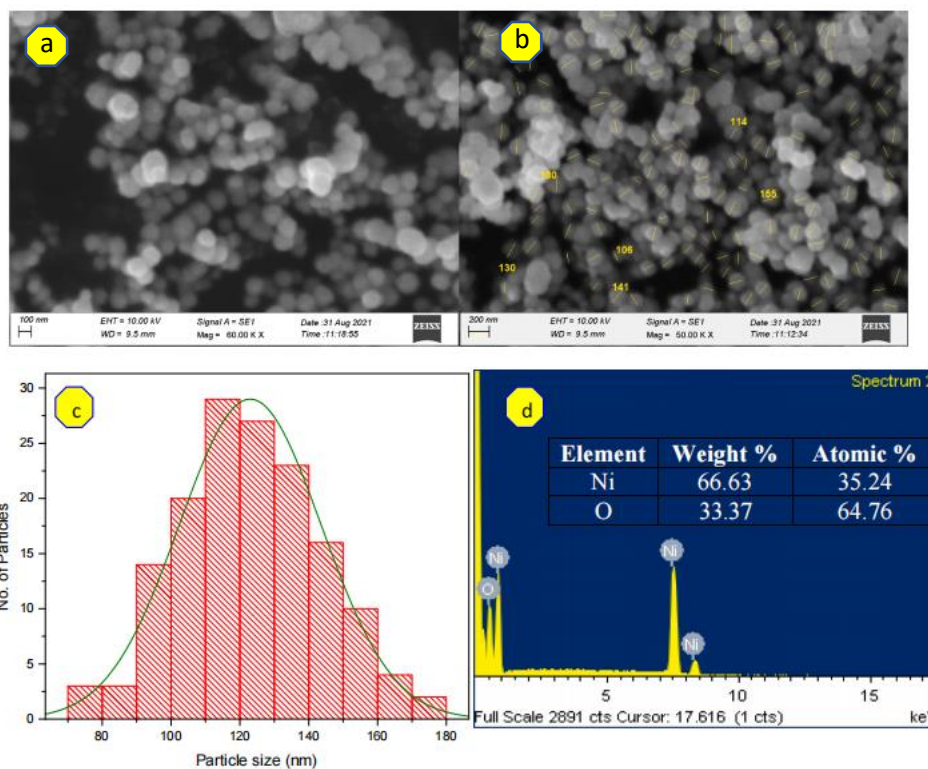


Figure 2.14: (a-b) SEM images, (c) Particle size distribution histogram, and (d) EDX analysis of NiO NPs (Haritha et al., 2022).

2.3.4 Green synthesis and characterization of NiO NPs using *Limonia acidissima* citrus fruit juice extract.

Kannan et al. (2020) investigated the production of NiO NPs utilizing fruit juice of *Limonia acidissima*. *Limonia acidissima* is typically called a wood apple, the juice consists of lactic acids and carbohydrates that function as potent reducing agents and perform the task of scavenging reactive oxygen species (ROS). This study is conducted using a microwave-assisted technique and the precursor salt utilized was nickel acetate. The microwave oven producing 850 W of radiation

was used to irradiate the solution for 15 minutes and calcinated at 600°C for 4 hours.

According to Figure 2.15, the NiO nanoparticles exhibited a maximum absorption peak at 322 nm. The band gap energy determined from the extension line from the Tauc plot was 3.41 eV, making it suitable for optoelectronic applications.

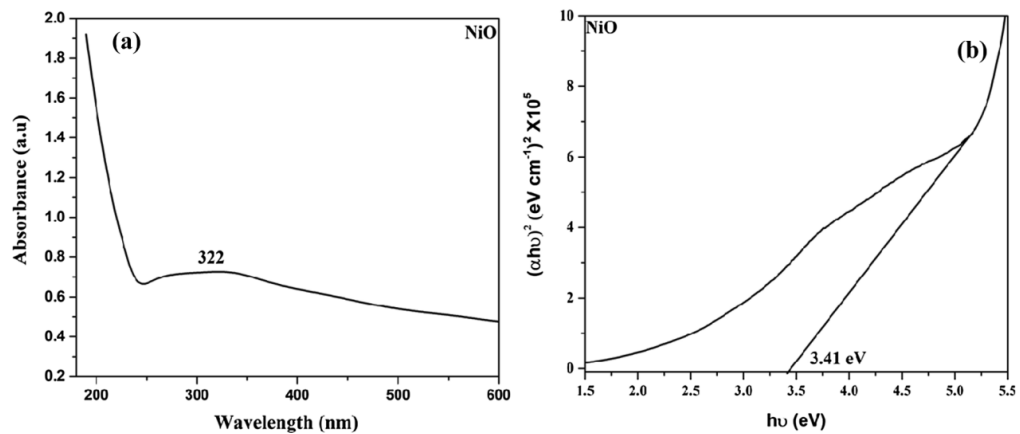


Figure 2.15: : (a) UV- Vis spectrum, and (b) Tauc plot of NiO NPs (Kannan et al., 2020).

The XRD diffractogram as illustrated in Figure 2.16 showed the cubic system of NiO NPs that matched with ICDD Card No. 89-7130 with lattice constant ($a=4.172 \text{ \AA}$) was obtained. The diffraction peaks obtained which corresponded to the Miller's index of (1 1 1), (2 0 0), (2 2 0), (3 1 1), and (2 2 2). The greater level of substance purity implied that no further compounds associated with secondary phases have been found. The mean crystallite size calculated was 20 nm.

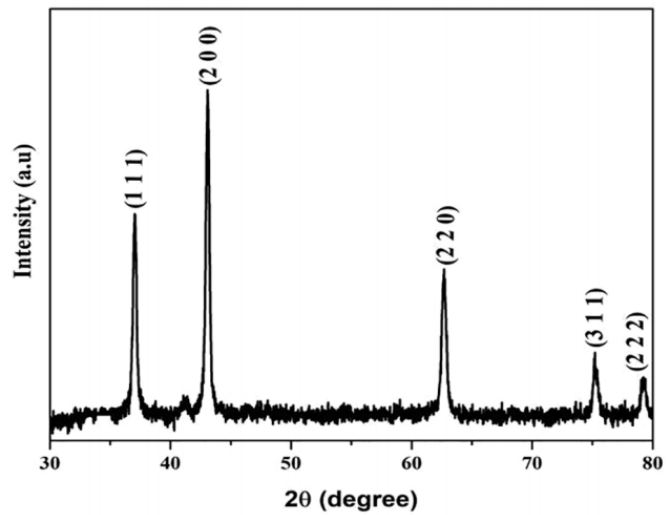


Figure 2.16: XRD pattern of NiO NPs (Kannan et al., 2020).

The SEM and TEM images in Figure 2.17 (a-b) showed that the NiO NPs were evenly dispersed and spherical with agglomeration occurring owing to the friction at the surfaces between the particles during combustion causing them to aggregate. Figure 2.17 (c) showed the atomic determination of NiO NPs revealing the existence of Ni and O elements with no additional peaks observed and pure NiO NPs were obtained.

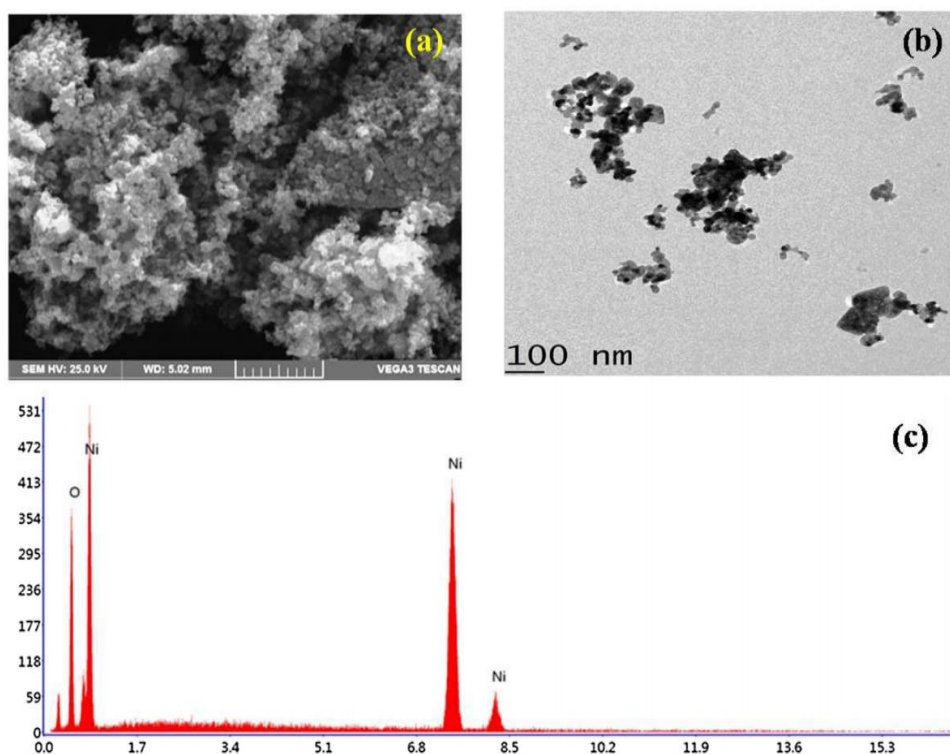


Figure 2.17: (a) SEM image, (b) TEM image, and (c) EDX analysis of NiO NPs (Kannan et al., 2020).

The FTIR spectrum of NiO NPs revealed in Figure 2.18, a broad O-H stretching band and bending mode of O-H were observed at 3450 cm^{-1} and 1640 cm^{-1} due to water molecules being absorbed. The diminished band at 2358 cm^{-1} indicated the C-H stretching. At 1382 cm^{-1} , the band suggested the existence of C-O bond. The key band identifying the presence of NiO NPs was observed at 428 cm^{-1} associated with the vibrational mode of NiO.

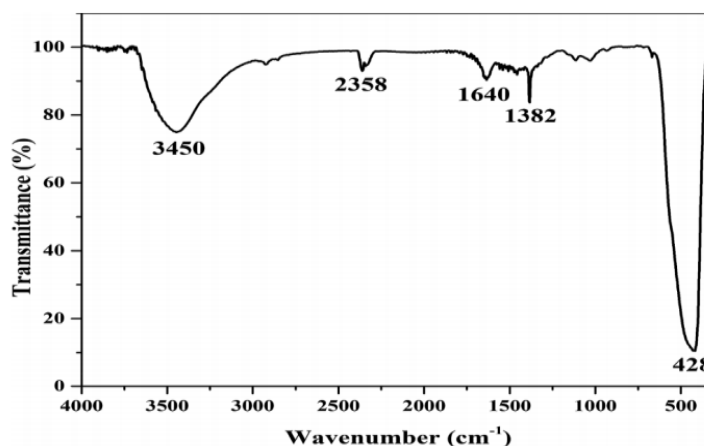


Figure 2.18: FTIR spectrum of NiO NPs (Kannan et al., 2020).

2.4 Concluding remarks

From these researches, it was proven that various precursor salts and parts of plants utilized in the green synthesis of NiO NPs depicted the variety of characterization results obtained. In this study, two different precursor salts such as nickel acetate tetrahydrate (Ni-A) and nickel nitrate hexahydrate (Ni-N) were utilized in the synthesis of NiO NPs. The effect of precursor salts was studied owing to a limited number of research available. In addition, the bark of *M. calabura* utilized in the synthesizing NiO NPs was less likely studied. The various precursor salts provide different environments and arrangements in the production of NiO NPs. As a result, different morphology, particle size, and crystal systems of NiO NPs could be obtained with the same bark extract. Table 2.2 depicted the summary of the different precursor salts and plant parts utilized in the synthesis of NiO NPs with their characterizations.

Table 2.2: Summary of the different precursor salts and plant parts utilized in the synthesis of NiO NPs with their characterizations.

Plant	Precursor salt	Plant parts	Absorption peak	Morphology	Particle size (nm)	Crystal system	References
<i>Annona muricata</i>	Nickel acetate	Peels	310	Spherical	20-90	Cubic	(Aminuzzaman et al., 2021)
<i>Euphorbia heterophylla</i>	Nickel nitrate	Leaves	321	Rhombohedral	12-15	Cubic	(Lingaraju et al., 2020)
<i>Averrhoa bilimbi</i>	Nickel nitrate	Peels	340	Spherical	110-120	Cubic	(Haritha et al., 2022)

<i>Limonia</i>	Nickel acetate	Fruit juice	322	Spherical	-	Cubic	(Kannan et al.,
<i>acidissima</i>							2020)

CHAPTER 3

MATERIALS AND METHODOLOGY

3.1 Materials

The barks of *M. calabura* were obtained from the parking zone of Block D, Universiti Tunku Abdul Rahman, Kampar, Perak, Malaysia. Nickel(II) acetate tetrahydrate (Ni-A) was utilized with the molecular weight of 248.84 g/mol and the CAS number was 6018-89-9. Furthermore, nickel(II) nitrate hexahydrate (Ni-N) was used with a molecular weight of 290.81 g/mol with its CAS number 13478-00-7. Both chemicals were analytical research (AR) grade and stored in the drying cabinet to prevent moisture absorption from air owe to their hygroscopic characteristics. They serve as precursor salts in synthesizing the NiO NPs. Lastly, deionized water was used in the cleaning of the barks to remove the dirt and impurities present. It also acts as a green solvent throughout this research.

3.2 Equipment

Table 3.1 lists the equipment utilized throughout this research.

Table 3.1: List of equipment utilized with their functions.

Equipment	Function
Aluminum foil	To ensure even heating of the mixture.
Analytical balance	To weigh the mass of the bark of <i>M. calabura</i> , precursor salts and NiO NPs obtained.
Centrifuge	To collect the supernatant of <i>M. calabura</i> extract after centrifugation process.
Ceramic crucible	To transfer the resulting paste into the furnace for calcination.
Desiccator	To store the NiO NPs for further characterization by avoiding moisture absorption.
Freeze dryer	To eliminate the water present in <i>M. calabura</i> extract.
Furnace	To calcinate the resulting paste into NiO NPs.
Grinder	To grind the dried bark of <i>M. calabura</i> into powdered form.

Hotplate	To heat the mixture by supplying heat energy.
Magnetic stirrer	To continuously stir the mixture steadily during the synthesis of NiO NPs.
Measuring cylinder	To measure the amount of <i>M. calabura</i> extract and deionized water utilized.
Mortar and pestle	To grind the NiO NPs and precursor salts with the KBr salts evenly during characterization.
Oven	To dry the bark of <i>M. calabura</i> before grinding it into powdered.
Retort stand and clamp	To secure the thermometer in a fixed position to observe the temperature changed.
Sonicator	To disperse the NiO NPs in the deionized water for characterization.
Thermometer	To monitor the change in temperature during the heating of the extract.

3.3 Instrument

Table 3.2 details the instruments employed in this research.

Table 3.2: List of instruments employed with their functions.

Instrument	Model	Function
Energy dispersive X-ray spectrometer (EDX)	Oxford Instruments X- Max 50mm ²	To determine the elemental composition of NiO NPs.
Field emission scanning electron microscope (FESEM)	JEOL JSM-6701F	To identify the morphology and particle sizes of NiO NPs.
Fourier transform infrared spectrometer (FTIR)	Perkin Elmer Spectrum Two	To determine the functional groups in the <i>M. calabura</i> extract, precursor salts, and synthesized NiO NPs.
UV-visible spectrophotometer (UV-Vis)	Thermo Fisher Scientific Genesys 180	To identify the maximum absorption wavelength and band gap energy of NiO NPs

X-ray Diffractometer (XRD)	Shimadzu XRD 6000	To study the crystallinity and crystallite size of NiO NPs.
-----------------------------------	-------------------	---

3.4 Overview of research methodology

The formation and characterization of NiO NPs are broken down into four parts as represented in Figure 3.1.

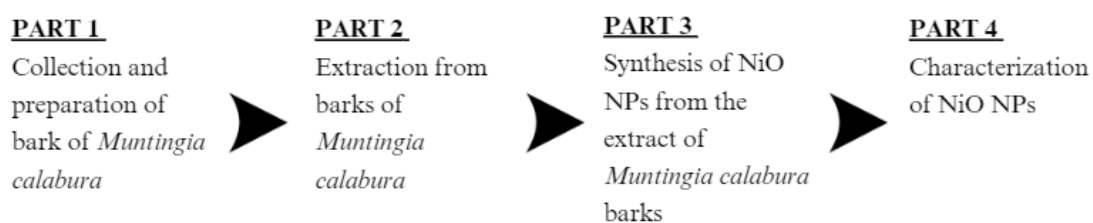


Figure 3.1: Overview of the methodology.

3.5 Experimental procedure

3.5.1 Collection and preparation of plant extracts

The barks of *M. calabura* were collected. Next, the barks of *M. calabura* were separated from the stems, followed by washing the peeled barks repeatedly with deionized water to eliminate the contaminants, dirt, and soil present on the surface of the barks. Next, the barks were cut into small pieces followed by drying in the oven at 40 °C until fully dried to remove moisture. The dried barks were ground into a fine powder and stored in a glass reagent bottle that was sealed with parafilm. The barks powdered was stored in a desiccator to prevent absorption of moisture. The flowchart is depicted in Figure 3.2. To prepare the *M. calabura* aqueous extract, 2.5 g of barks of *M. calabura* powdered was weighed using an analytical balance. The powder was then added to 100 mL of deionized water. The mixture was stirred and heated at 80 – 100 °C for about 45 minutes on a hot plate. Next, the extract was cooled to room temperature and subjected to centrifuging at the speed of 7000 rpm for 10 minutes to obtain the aqueous extract. The aqueous extract was transferred into centrifuge tubes and stored in the refrigerator at 4 °C for future synthesis. Figure 3.3 illustrates the flowchart outlining the preparation of *M. calabura* extract.



Figure 3.2: Flowchart for processing *M. calabura* bark into a powdered form.

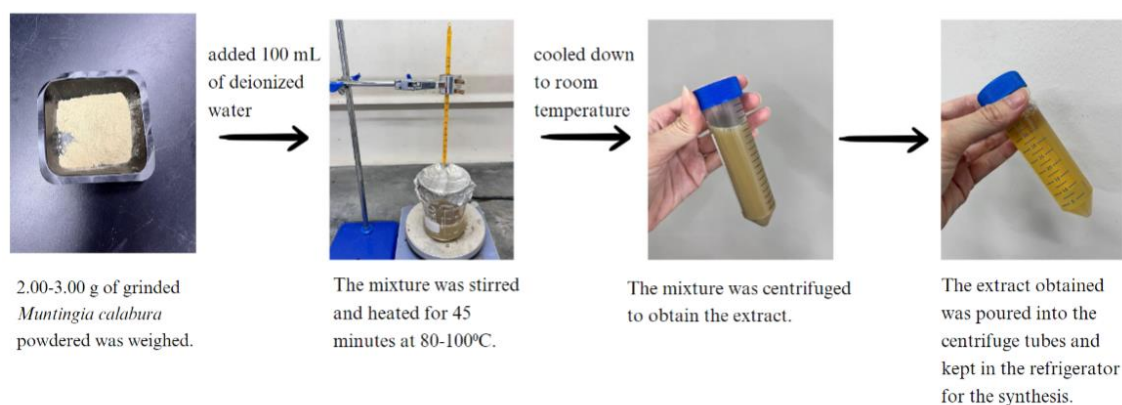


Figure 3.3: Extraction workflow diagram for *M. calabura* bark.

3.5.2 Green synthesis of nickel oxide nanoparticles

20 mL of plant extract was measured followed by dissolving 2 g of Ni-A in 20 mL of deionized water. The Ni-A solution was then added dropwise to the plant extract at 80-100 °C with constant stirring. The mixture was continued to heat

with constant stirring until a paste was formed. Next, the paste obtained was transferred to a ceramic crucible and calcinated at 450 °C for 2 hours in a furnace. The resulting black NiO powder was stored in a sealed airtight micro-sample tube in the desiccator for further characterization. A similar procedure was followed using Ni-N as precursor salt. The process flowchart for synthesizing NiO NPs is illustrated in Figure 3.4.

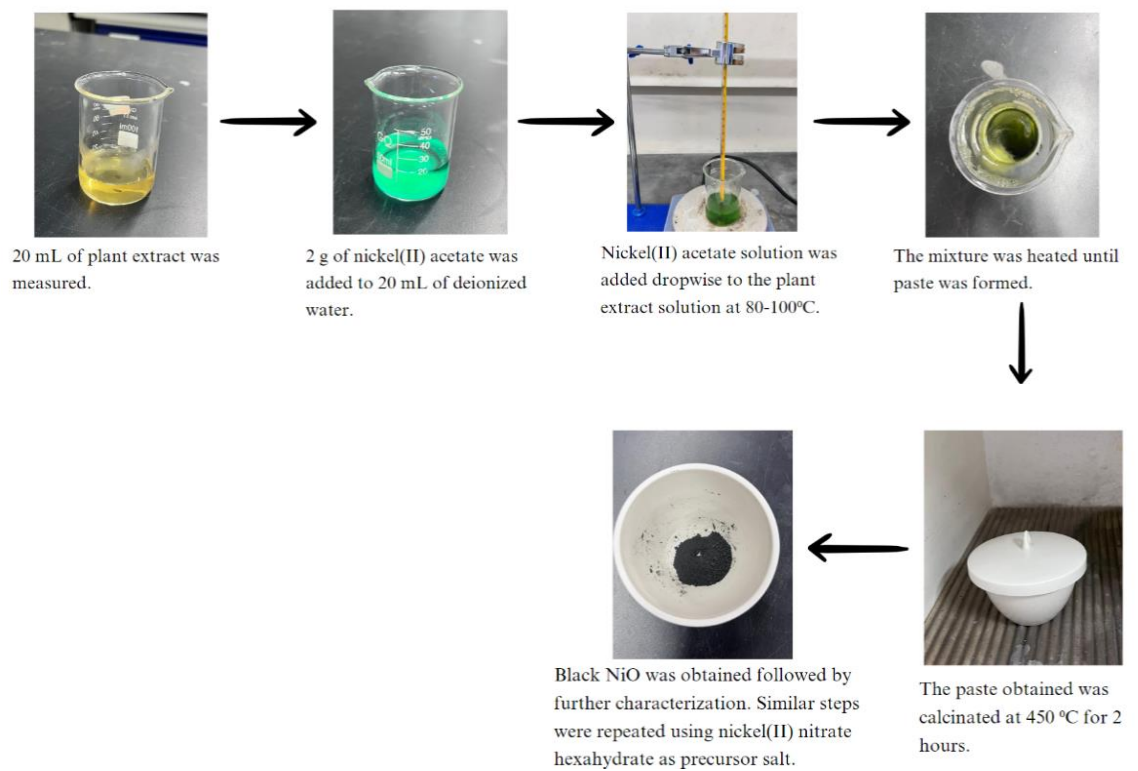


Figure 3.4: Overview of the NiO NPs synthesis process.

3.6 Percentage yield of synthesized nickel oxide nanoparticles

The mass of the precursor salt utilized and the NiO NPs obtained were weighed using an analytical weighing balance. The precursor salts used were Ni-A and Ni-N. The percentage yields of the synthesized NiO NPs utilizing different precursor salts were calculated using Equation 3.1.

$$\text{Percentage yield of NiO NPs} = \frac{\text{Mass of NiO NPs}}{\text{Mass of precursor salt}} \times 100\% \text{ ----- Equation 3.1}$$

3.7 Characterization of synthesized NiO NPs

The synthesized NiO NPs were characterized using Fourier Transform Infrared Spectroscopy (FTIR), Ultraviolet-Visible (UV-Vis) Spectroscopy, X-ray Diffraction (XRD), Field emission scanning electron microscope (FESEM), and Energy Dispersive X-Ray Spectroscopy (EDX).

3.7.1 Fourier Transform-Infrared Spectroscopy (FTIR)

The Fourier transform infrared spectrometer with the Perkin Elmer Spectrum Two model as depicted in Figure 3.5 was utilized to identify the functional groups in the *M. calabura* extract, precursor salts, and synthesized NiO NPs. The solid extract of *M. calabura* extract was obtained after freeze-drying for two days until the aqueous extract no longer contained water. Subsequently, all the solid samples were analyzed using the KBr pellet method. The KBr powdered was mixed evenly with finely ground solid extract *M. calabura*, precursor salts, and NiO NPs separately using mortar and pestle. Lastly, the solid sample was scanned from 4000 - 400 cm^{-1} .

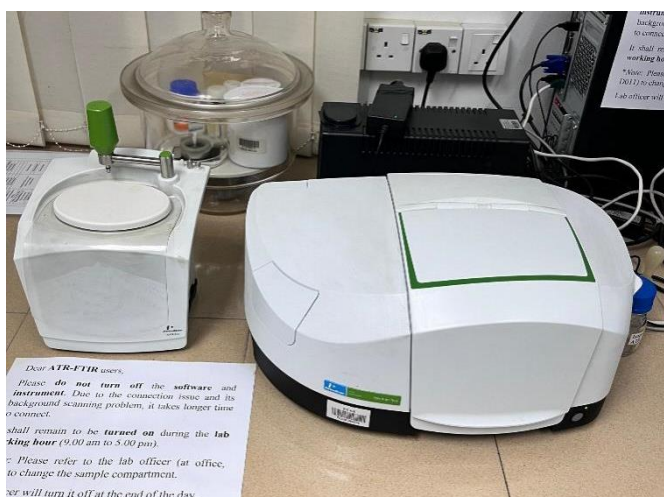


Figure 3.5: Perkin Elmer Spectrum Two model of FTIR analysis.

3.7.2 Ultraviolet-Visible Spectroscopy (UV-Vis)

A Thermo Fisher Scientific Genesys 180 UV-visible spectrophotometer as shown in Figure 3.6 was utilized to identify the optical and electronic characteristics of NiO NPs such as the maximum absorption wavelength (λ_{\max}) and band gap energy (E_g) of NiO NPs. About 2 mg of the synthesized NiO NPs were weighed and added to 10 mL of deionized water in a 15 mL centrifuge tube. The resulting sample solution was then sonicated for 10 minutes to ensure the NiO NPs were dispersed uniformly in the deionized water. Lastly, the solution was scanned over the wavelength range from 200-1000 nm.



Figure 3.6: Thermo Fisher Scientific Genesys 180 model of UV-Vis analysis.

According to the results obtained, the λ_{\max} values were used to determine the band gap energy within the NiO NPs using Equation 3.2. The unit conversion was needed as the calculated figures were in Joule (J) by multiplying with 1.60218×10^{-19} to obtain the unit in electron volt (eV) owing to 1 eV equals to 1.60218×10^{-19} J.

$$\text{Band gap energy, } E_g = \frac{hc}{\lambda} \text{ ----- Equation 3.2}$$

Where,

h = Planck's constant (6.626×10^{-34} Js)

c = Speed of light (3.00×10^8 ms⁻¹)

λ = Maximum absorption wavelength (nm)

3.7.3 Field Emission Scanning Electron Microscopy (FESEM) and Energy Dispersive X-ray Spectroscopy (EDX)

The morphology and particle sizes of NiO NPs were examined using a field emission scanning electron microscope (SEM), specifically the JEOL JSM-6701F model. Additionally, the atomic composition of the NiO NPs was examined with an energy dispersive X-ray spectrometer that was a small device attached to the SEM, particularly the Oxford Instruments X-Max 50mm² model. Figure 3.7 displayed both models of SEM and EDX instruments.



Figure 3.7: JSM-6701F and Oxford Instruments X-Max 50mm² models of SEM-EDX analysis.

3.7.4 X-ray Diffraction (XRD)

X-ray Diffractometer was used in the determination of the crystalline arrangement and crystallite size of NiO NPs, specifically the Shimadzu XRD 6000 model with Cu K α radiation ($\lambda = 1.5406 \text{ \AA}$) as depicted in Figure 3.8. The NiO NPs were scanned over a 2θ range from 10° to 85° at the scanning speed of 2.0000 %/min. The XRD peaks were compared to the reference data from the International Centre for Diffraction Data for matching. Furthermore, the crystallite size of NiO NPs can be determined through the Debye Scherrer equation as outlined in Equation 3.3.

$$D = \frac{K\lambda}{\beta \cos\theta} \text{ ----- Equation 3.3}$$

Where,

D = Crystallite size in diameter

K = Scherrer constant, 0.9

λ = Wavelength of X-ray source (Cu K α radiation= 1.5406 Å)

β = Full width at half maximum (FWHM) of the diffraction peak in radian 2θ

θ = Bragg's angle of diffraction

The value of FWHM of the diffraction peak was determined using Equation 3.4.

$$\beta = \frac{FWHM \text{ in } 2\theta \times \pi}{180^\circ} \text{ ----- Equation 3.4}$$



Figure 3.8: Shimadzu XRD 6000 model for XRD analysis.

CHAPTER 4

RESULTS AND DISCUSSION

4.1 Green Synthesis of NiO nanoparticles

In this study, NiO NPs were synthesized utilizing the bark of *M. calabura* with different precursor salts for instance Ni-A and Ni-N. The purpose of selecting these precursor salts was due to their solubility in bark extract and deionized water. As a result, the Ni²⁺ ions were activated and subsequently reduced to their metallic form. In addition, the high miscibility encourages quick nucleation and crystal development (Abdullah et al., 2024). The selection of other precursor salts such as nickel carbonate was not preferred owing to its immiscibility in bark extract and deionized water. Moreover, different anions such as acetate (CH₃COO⁻) and nitrate (NO₃⁻) ions affect the nucleation process in synthesizing the NiO NPs. Differences in solubility caused by the various anions affect supersaturation stages resulting in the extent and duration of nucleation (Abdullah et al., 2024). *M. calabura* was selected due to its rich phytochemical content such as alkaloids, flavonoids, saponins, tannins, and phenolic compounds that help serve as reducing, stabilizing, and capping agents (Pratiwi and Dewi, 2022). Moreover, *M. calabura* is widely available in Malaysia along the roadside.

In the preparation process, the bark of *M. calabura* was washed with deionized water to avoid any interference from ions with Ni²⁺ ions. The cleaned bark was then dried in an oven at 40°C mimic sunlight temperature to eliminate moisture. After drying, the bark was ground into a fine powder without any clumping. There were several methods to extract phytochemicals present in the bark of *M. calabura*. In this study, the decoction technique was utilized in the extraction of bark by fixing the amount of deionized water, and the process was sped up by applying heat. This method was suitable for miscible plant substances and highly thermally stable in heat (Abubakar and Haque, 2020).

In the synthesis of NiO NPs, the precipitation technique was used by adding dropwise the nickel solution to the bark extract. As a result, the processes of nucleation and growth were usually performed independently with nucleation producing seeds for later development. The existence of tiny particles kept the resultant two-phase system in a higher energy state. Ostwald ripening occurred as the development of bigger particles via combining with smaller soluble particles. This led to thermodynamic equilibrium being attained (Bastús et al., 2011). Nucleation can be visually monitored by observing a change in the colour of the sample solution from light to dark green (Azad et al., 2023). The mixture was then heated until the paste was formed to improve dispensing and stop cracks from forming when the NPs fuse (Zinn et al., 2013). The paste was transferred to the ceramic crucible and calcinated at 450 °C for 2 hours to convert into NiO NPs. Either by ambient oxygen or by the decomposition of phytochemicals that attach to the metals through electrostatic attraction. The nanomaterials form before the growth and stabilization period due to the

exposed nanoscale metal surface's heightened chemical responsiveness (Chan et al., 2024).

Figure 4.1 depicted the mechanism of synthesizing NiO NPs via a green synthesis pathway. The process of plant-assisted synthesis of NiO NPs considers the three subsequent stages (Imran and Rani, 2016):

- (i) The initiation phase includes the conversion of Ni^{2+} ions leading to the formation of metal nuclei through nucleation
- (ii) The developmental stage entails the spontaneous formation of tiny neighbouring NPs into more massive NPs which is known as Ostwald ripening, a procedure where NPs are generated directly via heterogeneous nucleation and subsequent growth followed by the further reduction of Ni^{2+} ions.
- (iii) The final stage determines the final morphology of NiO NPs. The final product is subjected to calcination in the air to obtain the NiO NPs.

The anions present after the dissolution process including acetate ions and nitrate ions assist in maintaining the stability of the synthesized NPs and their engagements with phytochemicals such as polyphenols extracted from bark extract lead to differences in the developmental and final stages. The phytochemicals present induce metals to generate their metal oxides and facilitate their progression to the development and stabilization stages. As a result, NiO NPs with a specific form are generated during the final process at

the annealing temperatures by attaching metal ions to oxygen (Abdullah et al., 2024).

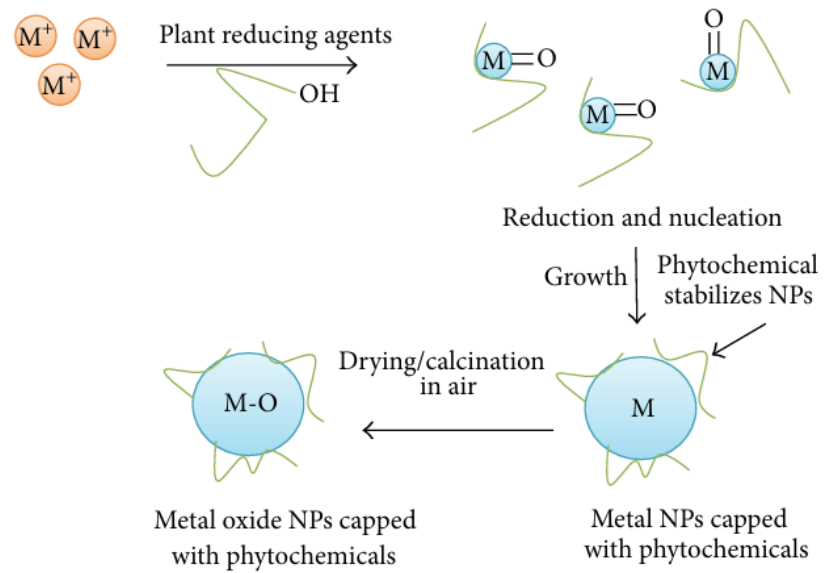


Figure 4.1: Mechanism of synthesizing NiO NPs via a green synthesis pathway (Imran and Rani, 2016).

4.2 Percentage yield of synthesized nickel oxide nanoparticles (NiO NPs)

The percentage yield obtained for NiO NPs produced from two precursor salts was tabulated in Table 4.1.

Table 4.1: Percentage yield of synthesized NiO NPs from two precursor salts.

Precursor salts	Percentage yields of NiO nanoparticles
Nickel(II) acetate tetrahydrate	$\frac{0.5141 \text{ g}}{2.0013 \text{ g}} \times 100\% = 25.7\%$
Nickel(II) nitrate hexahydrate	$\frac{0.4071 \text{ g}}{2.0008 \text{ g}} \times 100\% = 20.3\%$

It was noted that the yield of NiO nanoparticles synthesized using different precursor salts was relatively low. Several factors contributed to this outcome. In this study, the use of young *M. calabura* bark may have impacted the phytochemical content compared to older bark. Additionally, the low concentration of phytochemicals in the bark extract may have reduced the efficiency of converting Ni²⁺ ions to their metallic form, resulting in lower yields of NiO NPs. The extraction time for the bark could also influence the quantity of phytochemicals extracted owing to the solubility of young bark material might be less favorable. Phytochemical screening could be conducted to identify the phytochemicals present in the young bark and extending the extraction duration may help increase the quantity of phytochemicals obtained.

4.3 Characterization of synthesized NiO NPs

The black NiO NPs synthesized utilized Ni-A and Ni-N as precursor salts were characterized using Fourier Transform Infrared Spectroscopy (FTIR), UV-Visible Spectroscopy (UV-Vis), X-ray Diffraction (XRD), Field Emission Scanning Electron Microscopy (FESEM) and Energy Dispersive X-ray Spectroscopy (EDX).

4.3.1 Fourier-Transform Infrared Spectroscopy (FTIR)

The FTIR examination was conducted over a wavenumber range of 4000 - 400 cm^{-1} to detect the functional groups present in the *M. calabura* bark extract and the synthesized NiO NPs from two different precursor salts, Ni-A and Ni-N. The FTIR spectra of the NiO NPs synthesized by two precursor salts are shown in Figures 4.2 and 4.4.

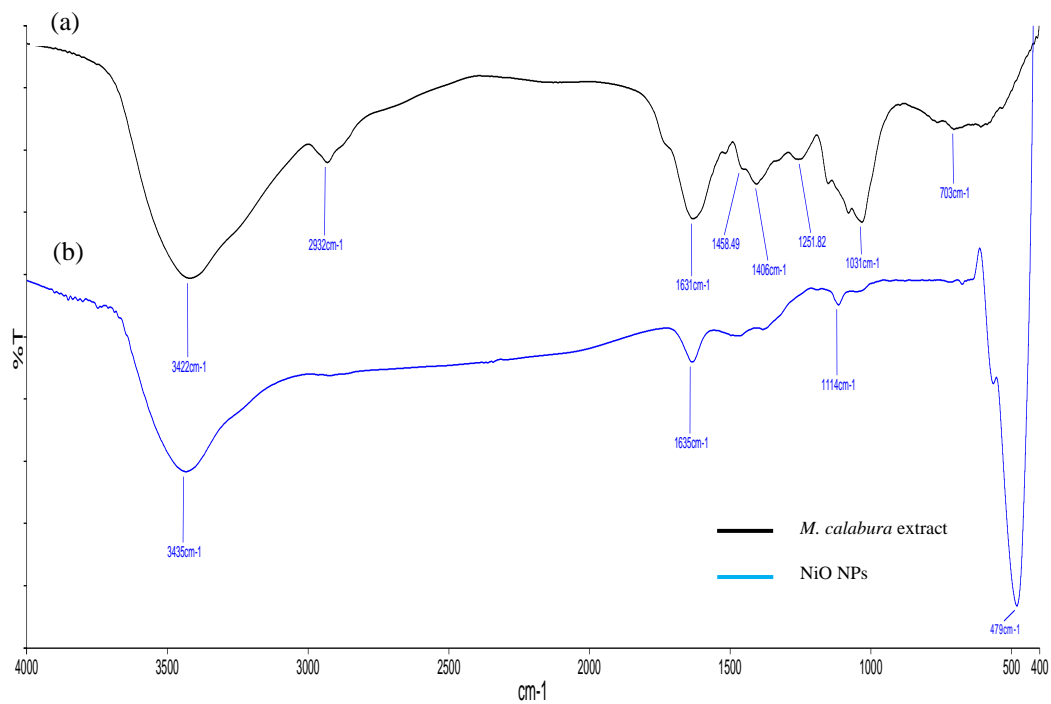


Figure 4.2: FTIR spectra of (a) bark extract of *M. calabura* (b) NiO NPs using Ni-A as precursor salt.

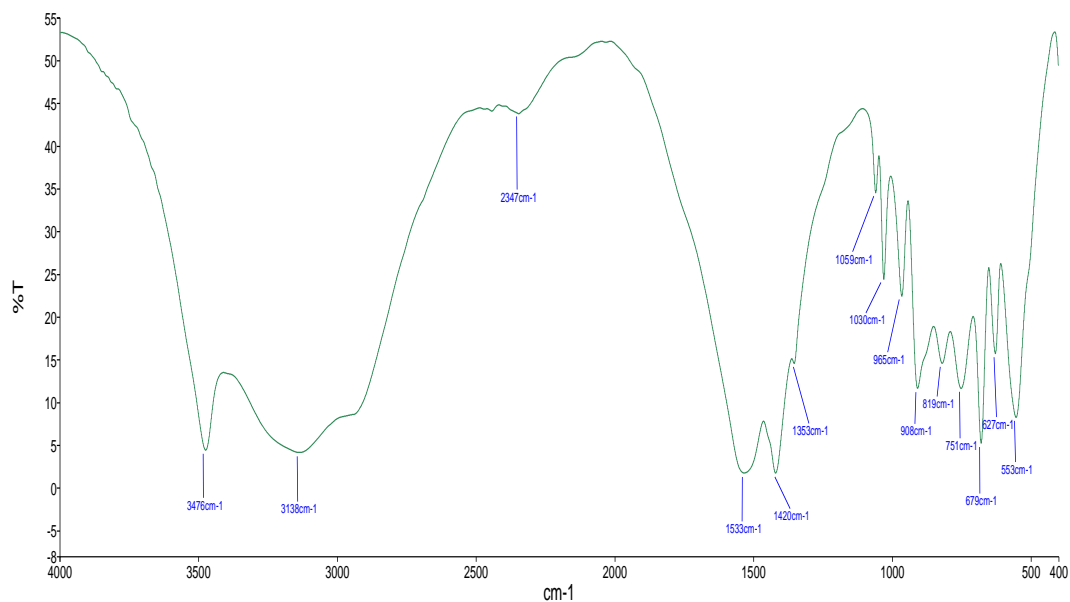


Figure 4.3: FTIR spectrum of Ni-A.

As depicted in Figure 4.2(a), the aqueous *M. calabura* bark extract exhibits several characteristic peaks corresponding to various functional groups. A broad band observed at 3422 cm^{-1} suggests the presence of O-H stretching, likely due to phenol or alcohol groups. The band at 2932 cm^{-1} corresponds to C-H stretching, which is typical of alkanes. Additionally, the band at 1631 cm^{-1} is attributed to C=O stretching, indicating the presence of flavonoids. The band at 1406 cm^{-1} is associated with symmetric COO^- stretching, confirming the presence of carboxylate groups (Selvanathan et al., 2021). A band at 1251.82 cm^{-1} corresponds to C-O stretching, commonly found in alcohols, esters, or ethers. Lastly, the band at 1031 cm^{-1} is attributed to C-N stretching, suggesting the presence of amines or amides (Selvanathan et al., 2021). According to Wahid Wahab et al. (2018), both O-H stretching and C=O stretching are associated with compounds found in flavonoids, tannins, terpenoids, saponins, and polyphenols as depicted in Figure 4.4. According to Ritu et al. (2023), the alkaloids in the plant extract function as a reducing agent that assists in the reduction of Ni^{2+} ions. The presence of flavonoids and terpenes serves as stabilizing agents and capping agents. The stability of the interface between the nanoparticles and their formation medium is assured by these capping ligands. In colloidal synthesis, capping compounds are essential stabilizers since they inhibit NPs development beyond a certain point and prevent them from aggregating or coagulating (Javed et al., 2020). They are also secondary metabolites that serve as a natural defensive mechanism and confer therapeutic characteristics to plants (Uddin et al., 2021).

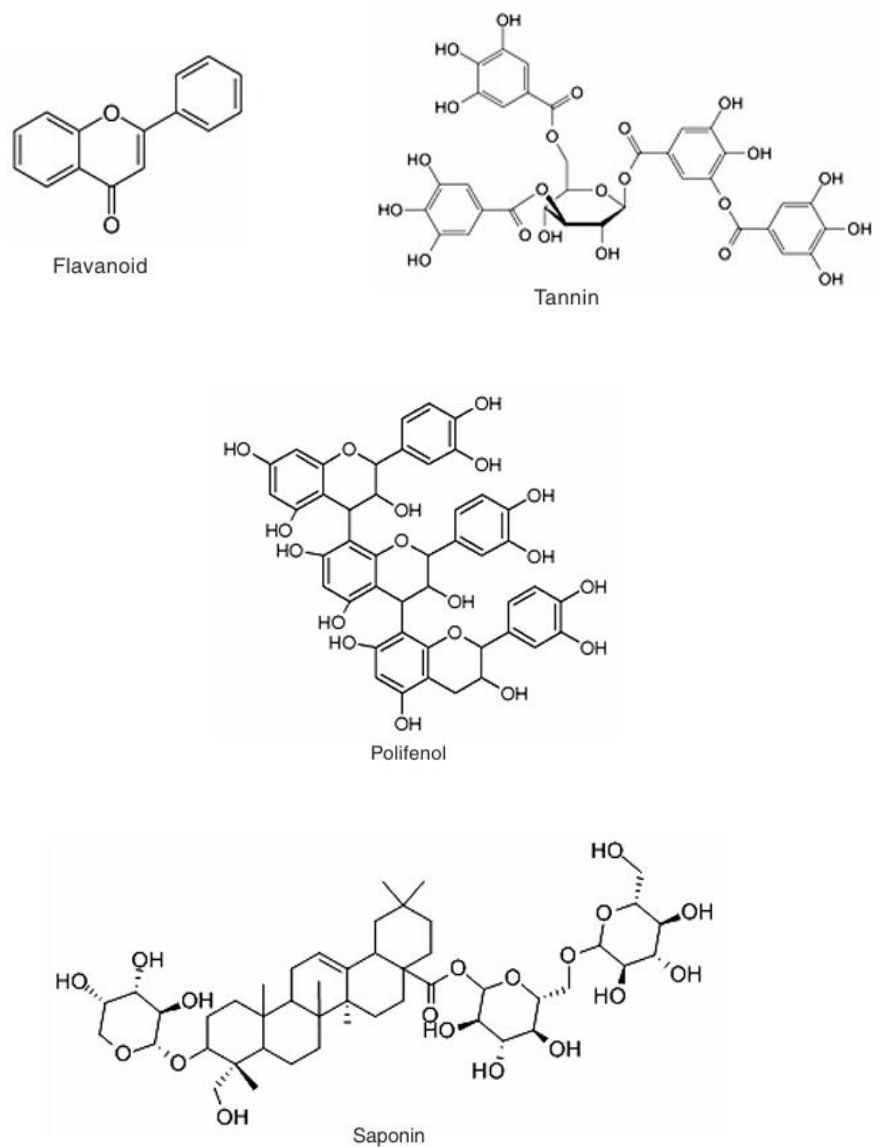


Figure 4.4: Structures of compounds that contribute both O-H stretching and C=O stretching (Wahid Wahab et al., 2018).

Based on Figure 4.2 (b), the O-H stretching band observed at 3435 cm^{-1} was due to the nature of KBr which is hygroscopic, and easily absorbs water from the atmosphere during the preparation of the KBr pellet for analysis (Gordon et al., 2010). Additionally, the bands detected at 1635 cm^{-1} and 1141 cm^{-1} were attributed to C=O stretching and C-O stretching, respectively owing to the

absorption of atmospheric carbon dioxide by the KBr pellet prepared (El-Kemary et al., 2013). Lastly, the significant band that indicates the presence of NiO NPs was observed at 479 cm^{-1} , indicating the NiO stretching vibrational mode (Wardani et al. 2019). Table 4.2 summarizes the FTIR spectra for the bark extract of *M. calabura*, Ni-A, and NiO NPs (Ni-A).

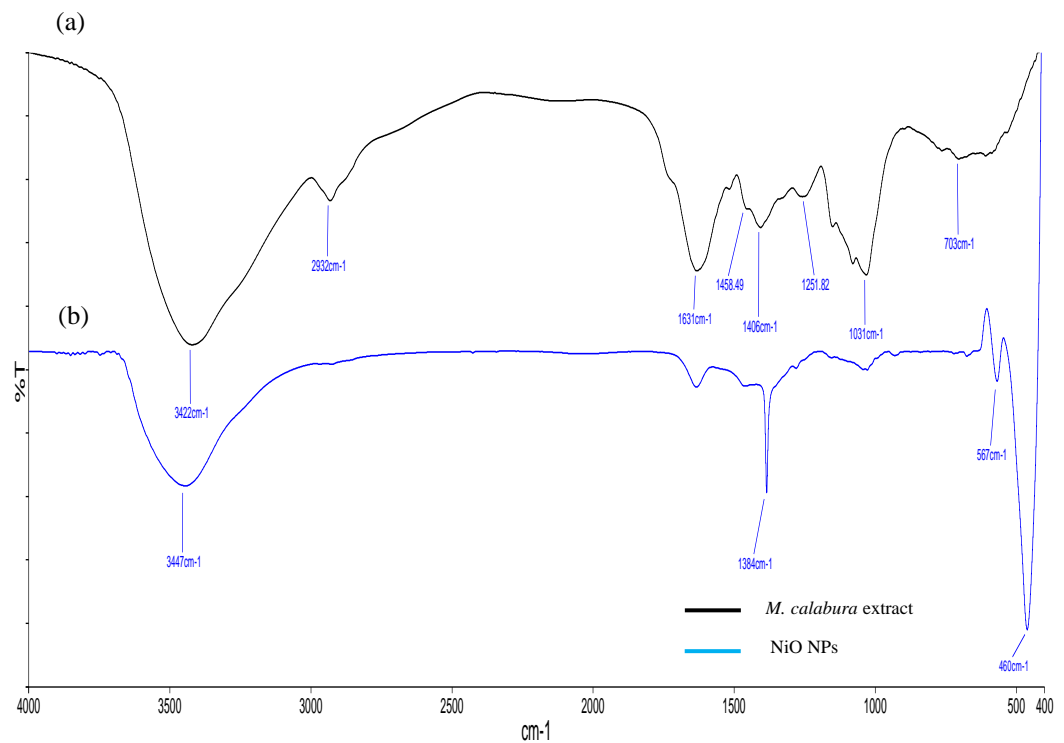


Figure 4.5: FTIR spectra of (a) bark extract of *M. calabura* (b) NiO NPs using Ni-N as precursor salt.

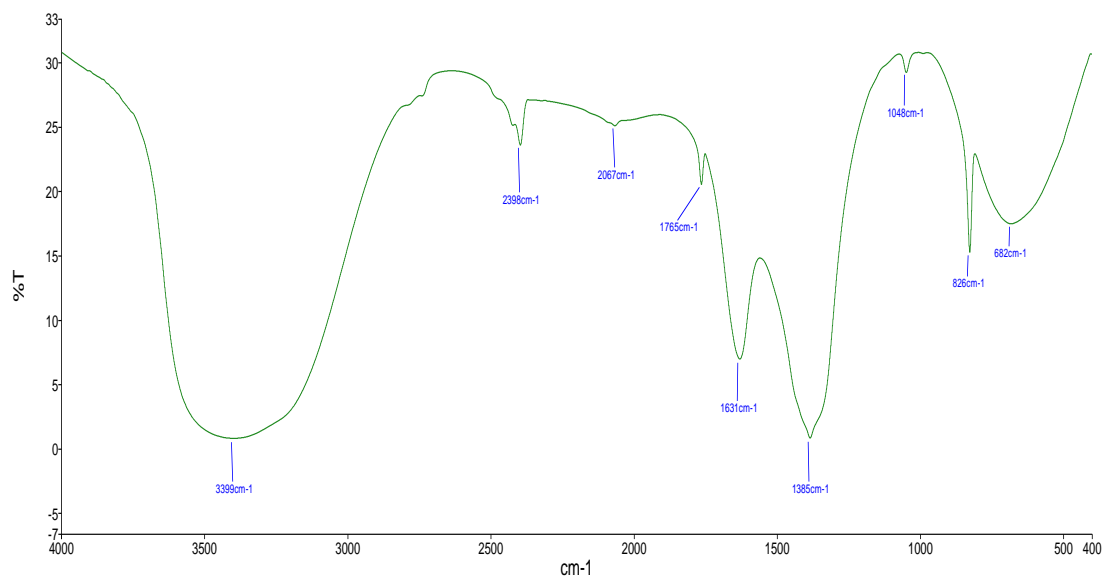


Figure 4.6: FTIR spectrum of Ni-N.

According to Figure 4.5 (b), the observed band at 460 cm⁻¹ is associated with the stretching vibrations of NiO bonds (Imran Dinand Rani, 2016; El-Kemary et al., 2013). This is attributed to the observed range of 780-480 cm⁻¹, which signifies the presence of metal-oxygen vibrational modes, indicating the formation of NPs (Haritha et al., 2022). In Table 4.2, the FTIR spectra of bark extract of *M. calabura*, Ni-N, and NiO NPs (Ni-N) are summarized.

Table 4.2: Summary of FTIR spectra of bark extract of *M. calabura*, Ni-A, NiO NPs (Ni-A), Ni-N, and NiO NPs (Ni-N).

	Wavenumber (cm ⁻¹)				
	<i>M. calabura</i>	Ni-A	NiO NPs (Ni-A)	Ni-N	NiO NPs (Ni-N)
ν (O-H)	3422	3476	3435	3399	3447
ν (C-H)	2932	3138 (s) 1353 (δ)	-	-	-
ν (CO ₂)	-	-	-	2398 (as)	
ν (C=O)	1631	1533 (as) 1420 (s)	1635	1765	1633.69

$\nu(NO_3^-)$	-	-	-	1631 (as)	-
				1385 (s)	
$\nu(COO^-)$	1406	-	-	-	-
$\nu(C-O)$	1251.82	-	1141	-	1384
$\nu(C-N)$	1031	-	-	-	-
$\nu(NiO)$	-	-	479	-	460

4.3.2 Ultraviolet-Visible Spectroscopy (UV-Vis)

Several techniques cannot discriminate between dispersed and aggregated particles, preserve sample integrity, or allow real-time nanomaterial (NM) size analysis. On the other hand, UV-Vis spectroscopy is a frequently utilized method offering a quick, non-invasive real-time assessment of NM dimension, concentration, and aggregation condition. It is also an easy-to-use, low-cost method that requires little sample preparation, which makes it a vital instrument that is frequently applied in a variety of lab settings and academic fields (Quevedo et al., 2021). It is a highly utilized technique for characterizing nanoparticles and evaluating the energy arrangements and optical properties of nanoparticles (Sagadevan and Podder, 2015). It allows for accurate measurement of their characteristics such as maximum absorbance and peak wavelength (λ_{\max}) (Quevedo et al., 2021).

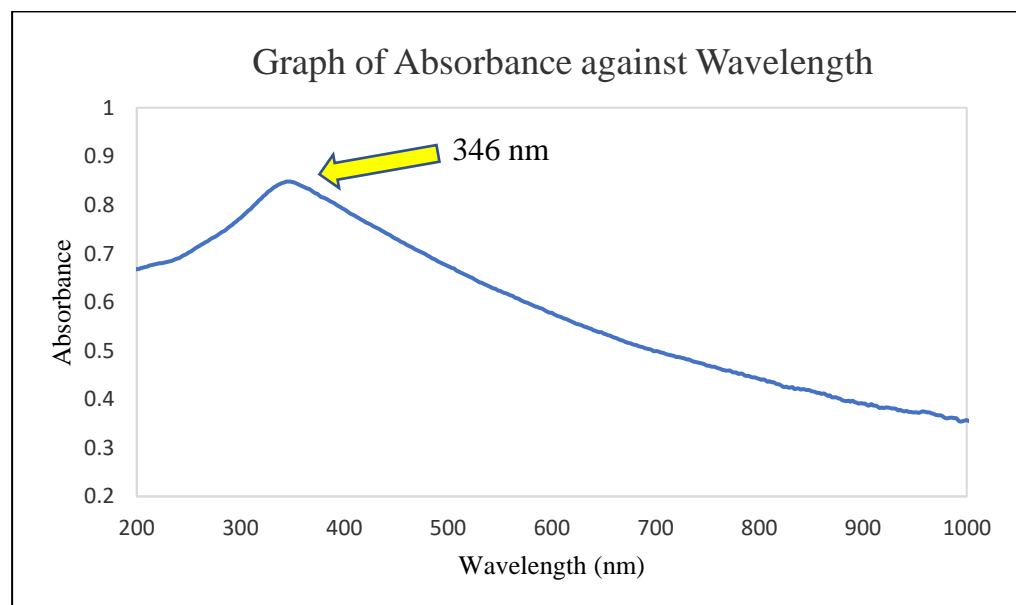


Figure 4.7: Absorption spectrum of synthesized NiO NPs from Ni-A range from 200 nm to 1000 nm.

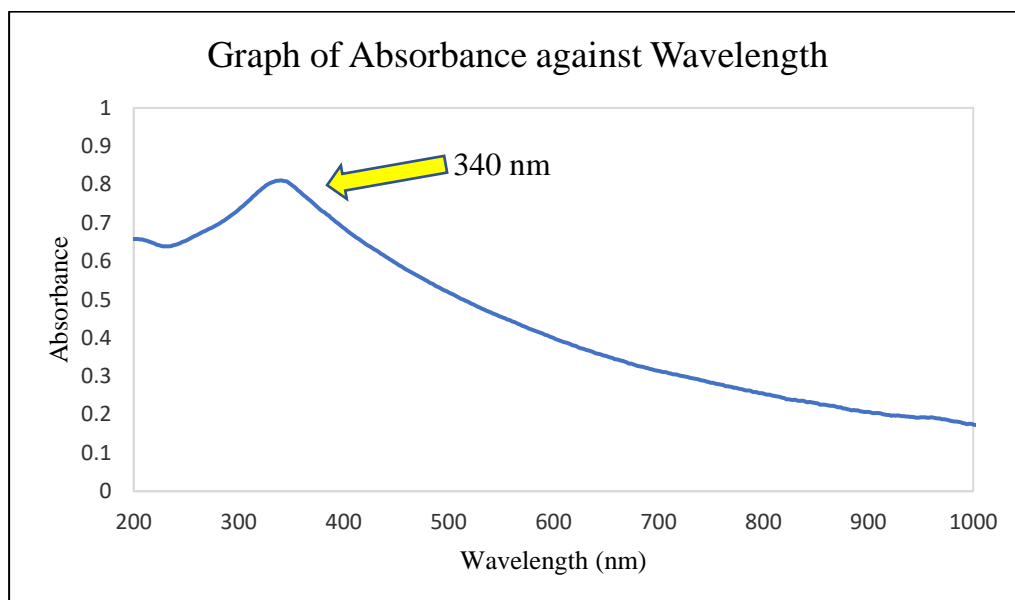


Figure 4.8: Absorption spectrum of synthesized NiO NPs from Ni-N range from 200 nm to 1000 nm.

As illustrated in Figure 4.7, the λ_{\max} of NiO NPs synthesized with Ni-A as precursor salt was 346 nm. It is supported by the findings from Haider et al. (2020), where the λ_{\max} obtained from NiO NPs synthesized using the extract of *Zingiber officinale* and *Allium sativum* was 350 nm. Referring to Figure 4.8, the NiO nanoparticles synthesized using Ni-N as the precursor salt exhibited λ_{\max} of 340 nm. This is agreed with the studies from Haritha et al. (2022) which used peels of *Averrhoa bilimbi* fruits which was 340 nm. The blue shift occurred as observed for λ_{\max} of NiO NPs synthesized with Ni-A (346 nm) and Ni-N (340 nm). Typically, the λ_{\max} decreases with decreasing particle size. This is owing

to the photo-generated electron-hole carriers' quantum confinement effect (Sagadevan and Podder, 2015).

The vast surface area and small size of NiO NPs improve their absorption capacity and photon-capturing efficiency. The noticeable UV absorption that is apparent is caused by the adsorption band of NiO semiconductors (Sabouri et al., 2021). The notable absorbance peaks obtained from two precursor salts correspond to the electron transfer in NiO NPs from the valence band to the conduction band, particularly from 2p orbital from O to 3d orbital of Ni. These peaks result from the movement of charge from the ligand to the metal (Haritha et al., 2022). The formula for calculating the bandgap (E_g) of NiO nanoparticles is shown below.

$$(\mu h\nu)^n = A (h\nu - E_g)$$

which μ is the absorptivity coefficient, $h\nu$ represents the energy of photons, A corresponds to a constant, E_g indicates band gap energy and n could be equivalent to 2 or $\frac{1}{2}$ for direct and indirect transitions respectively (Sabouri et al., 2021).

The E_g for NiO nanoparticles synthesized using Ni-A and Ni-N as the precursor salts were found to be 3.58 eV and 3.64 eV. The increase in E_g was due to the reduction in particle size as this is agreed that a blue shift occurred (Sabouri et al., 2021). Additionally, these measurements indicate that the NiO NPs produced are direct semiconductors (Sabouri et al., 2021).

A hole is created in the valence band (VB) and an exciton which is a pair of an electron and a hole coupled by Coulomb contact is produced when a semiconductive material absorbs a photon with energy that meets or exceeds its E_g (Rabouw and de Mello Donega, 2016). Quantum confinement effects become noticeable when the NPs size approximates the exciton Bohr radius, which is the gap between an electron and a hole. In simple terms of explanation, nanomaterials begin exhibiting quantum characteristics as their sizes decrease and their quantum effects get stronger. The charge carriers including electrons and holes are trapped inside the material's minuscule sizes in these quantum structures (Joudeh and Linke, 2022). As a result, as the NPs size decreases, discrete energy levels start developing close to the band boundaries, and the bandgap, known as the HOMO–LUMO energy gap increases as depicted in Figure 4.9 (Rabouw and de Mello Donega, 2016).

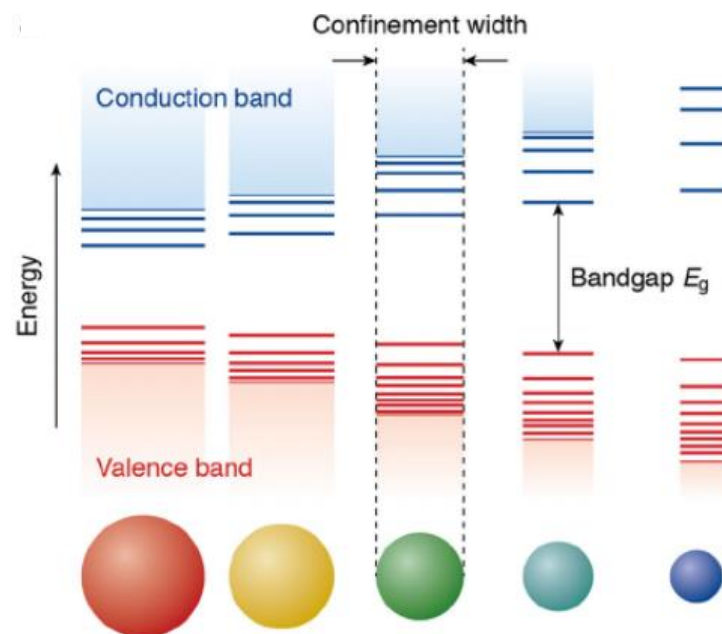


Figure 4.9: Quantum confinement effects experienced by semiconductor nanoparticles as size decreases (Rabouw and de Mello Donega, 2016).

4.3.3 Field Emission Scanning Electron Microscopy (FESEM)

An electron gun emits an electron beam for scanning electron microscopy (SEM), which proceeds to focus through several lenses and travels vertically across the microscope until it strikes the sample. The sample produces electrons and X-rays upon collision which the detectors receive. The X-rays and scattered electrons are collected by these detectors that are used to provide a three-dimensional picture of the material. SEM provides significant details on the dimension, shape, aggregation, and distribution of NPs (Joudeh and Linke, 2022).

As illustrated in Figures 4.10 and 4.11, the synthesized NiO NPs from two precursor salts exhibited spherical shapes, and particle size obtained for NiO synthesized utilizing Ni-A and Ni-N as the precursor salts were 44.7 - 65.6 nm and 37.8 - 61.6 nm respectively. Moreover, agglomeration of NiO NPs in the SEM images was observed. Agglomeration in nanoparticles is the process by which particles adhere together by weak interactions (Gosens et al., 2010). The small dimensions of the nanoparticles encourage the agglomeration of NPs. Additionally, larger particle sizes possess smaller surface areas, which lowers the surface free energy. Consequently, the particles clump together which leads to agglomeration occurred (Mahadevaswamy et al., 2022). Agglomeration can be reduced by modifying the hydrophilicity or hydrophobicity of the particles, raising their zeta potential to enhance their repulsive forces, or altering the pH and ionic concentration of the suspension medium (Joudeh and Linke, 2022).

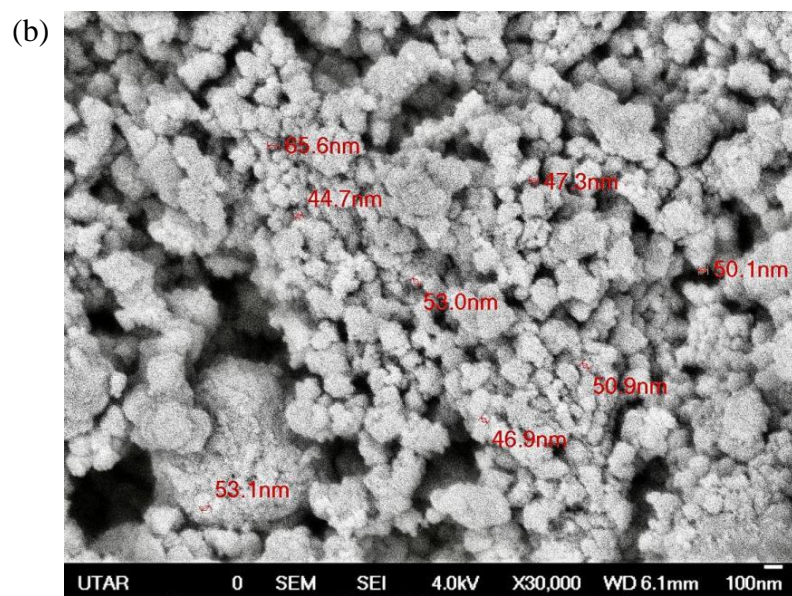
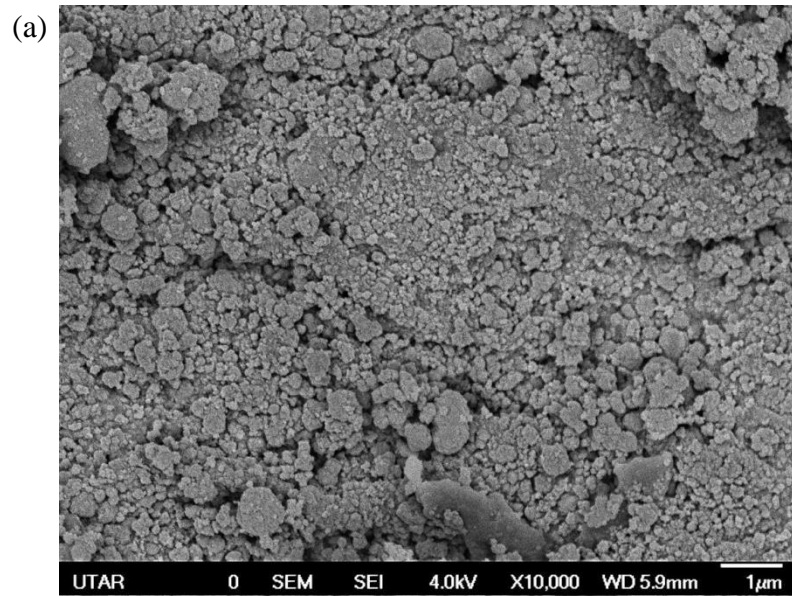


Figure 4.10: FESEM images of NiO NPS synthesized by Ni-A as precursor salt at magnifications of (a) 10000× (b) 30000×

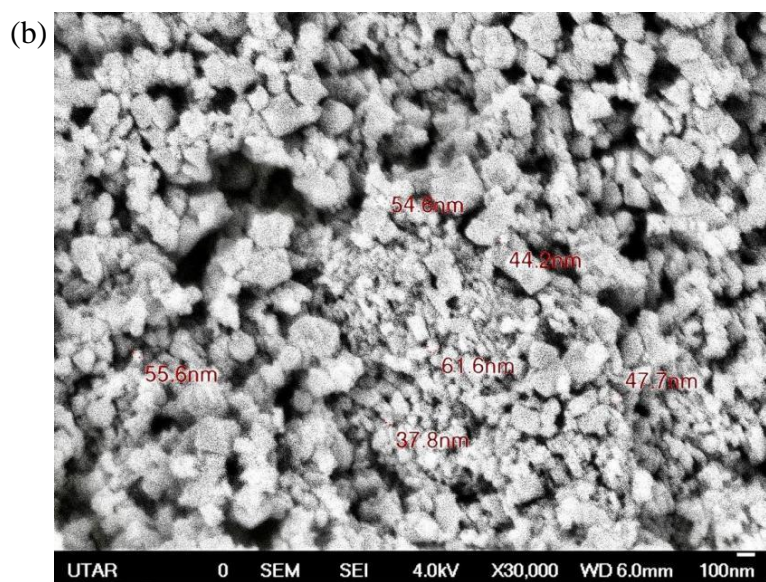
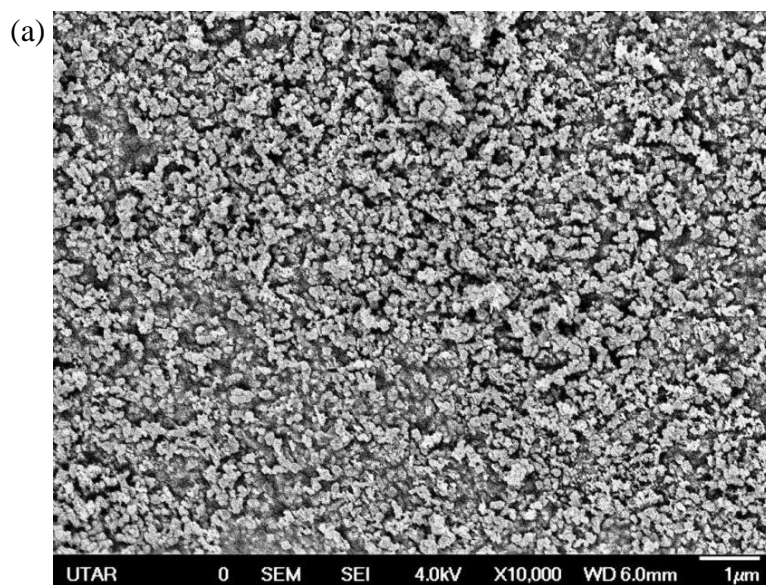


Figure 4.11: FESEM images of NiO NPS synthesized by Ni-N as precursor salt at magnifications of (a) 10000× (b) 30000×

4.3.4 Energy Dispersive X-ray Spectroscopy (EDX)

EDX is a small gadget that plugs into an existing SEM and allows both morphological characterization and chemical composition analysis utilizing EDX at the same time (Joudeh and Linke, 2022). It uses an electron beam to irradiate the material. The electron beam dislodges the electrons in the inner shell as it hits the surface of the sample. This causes the electrons in the outer shell to transition to occupy the ensuing vacancies and this change generates X-rays. Compositional analysis is made possible by the distinctive X-ray patterns that each element generates owing to its distinct atomic structure (Groarke et al., 2021). Without providing exact quantification, EDX gives qualitative compositional data that identifies the chemical constituents contained in a sample. Nonetheless, an approximate estimation of the relative proportion of each element in the sample may be obtained from the peak strengths (Nasrollahzadeh et al., 2019).

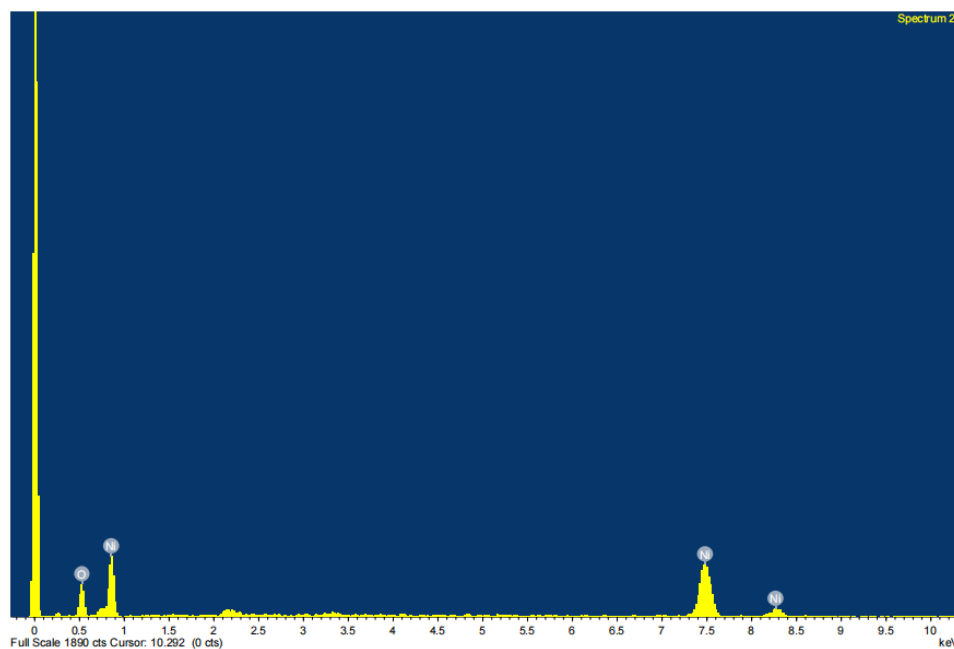


Figure 4.12: EDX spectrum of the synthesized NiO NPs using Ni-A as precursor salt.

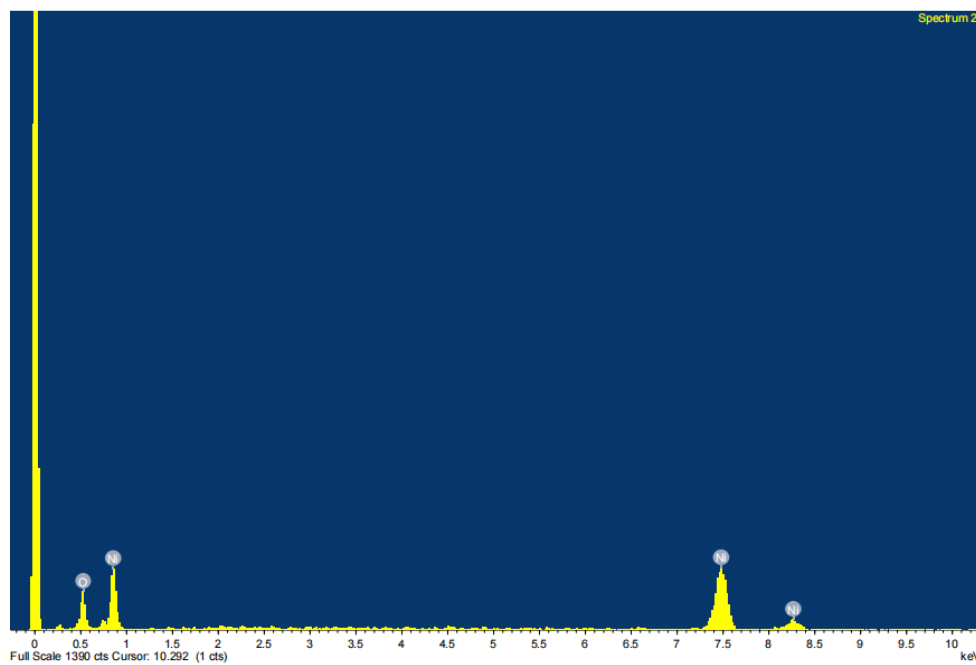


Figure 4.13: EDX spectrum of the synthesized NiO NPs using Ni-N as precursor salt.

Table 4.3: EDX analysis of weight percent with its atomic percent of the elements present in NiO NPs using Ni-A and Ni-N as precursor salts.

NiO (Ni-A)			NiO (Ni-N)		
Element	Weight percent (%)	Atomic percent (%)	Element	Weight percent (%)	Atomic percent (%)
Nickel (Ni)	66.74	35.36	Nickel (Ni)	67.74	36.40
Oxygen (O)	33.26	64.64	Oxygen (O)	32.26	63.60
Total	100.00	100.00	Total	100.00	100.00

From the EDX image as depicted in Figure 4.12, the NiO NPs obtained using Ni-A are composed of only Ni and O elements which are 66.74% and 33.26% respectively by weight percent as tabulated in Table 4.3. Similarly, the NiO NPs produced using Ni-N as illustrated in Figure 4.13, consist of Ni and O elements which are 67.74% and 32.26% respectively as summarized in Table 4.3. This confirms that both sets of NiO NPs synthesized from different precursor salts are free from impurities and contain only Ni and O elements.

4.3.5 X-ray Diffraction (XRD)

This method entails pointing X-rays at a substance and analyzing the angles and intensities of the X-rays that scatter as they depart the substance (Epp, 2016). The analysis was carried out to evaluate the configuration, crystalline structure, lattice variables, pureness, and dimension of the NPs. It also served to verify the NPs' phase. The various phases comprised in the synthesized NPs were determined by comparing the peak locations (2θ values) in the XRD pattern against the standard information gathered from the International Centre for Diffraction Data (ICDD) card (Abraham et al., 2020). Three numbers denoted as Miller indices are used to describe a collection of planes as a surface is created when the crystalline solid cuts at a certain lattice plane (Vattuone et al., 2018).

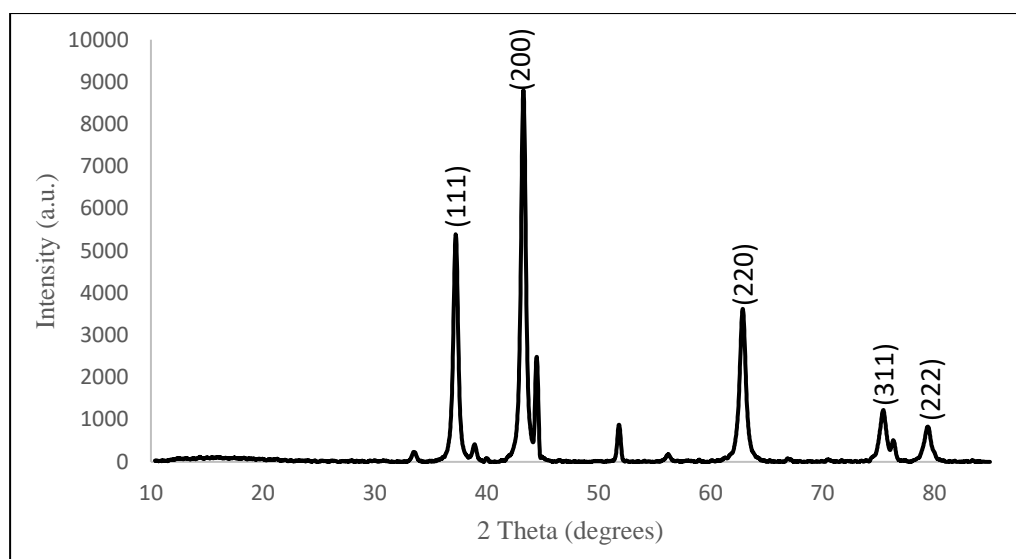


Figure 4.14: XRD diffractogram of the synthesized NiO NPs using Ni-A as precursor salt.

According to Figure 4.14, the crystalline nature of NiO NPs synthesized using Ni-A was observed. The diffraction peaks located at 2θ were detected at 37.27° , 43.32° , 62.84° , 75.4° , and 79.34° that matched the crystallographic planes of (111), (200), (220), (311), and (222) respectively. The diffraction peaks were 96.0 % matched with ICDD Card No. 01-071-6724 as depicted in Appendix C. In addition, the synthesized NiO NPs exhibited the crystal system of trigonal with hexagonal axes (rhombohedral) with the space group of R-3m, and the lattice parameters obtained were $a = 2.9549 \text{ \AA}$ and $c = 7.2320 \text{ \AA}$. The degree of crystallinity exhibited by NiO NPs was 12.41 % with the remaining 87.59 % corresponding to the content of amorphous.

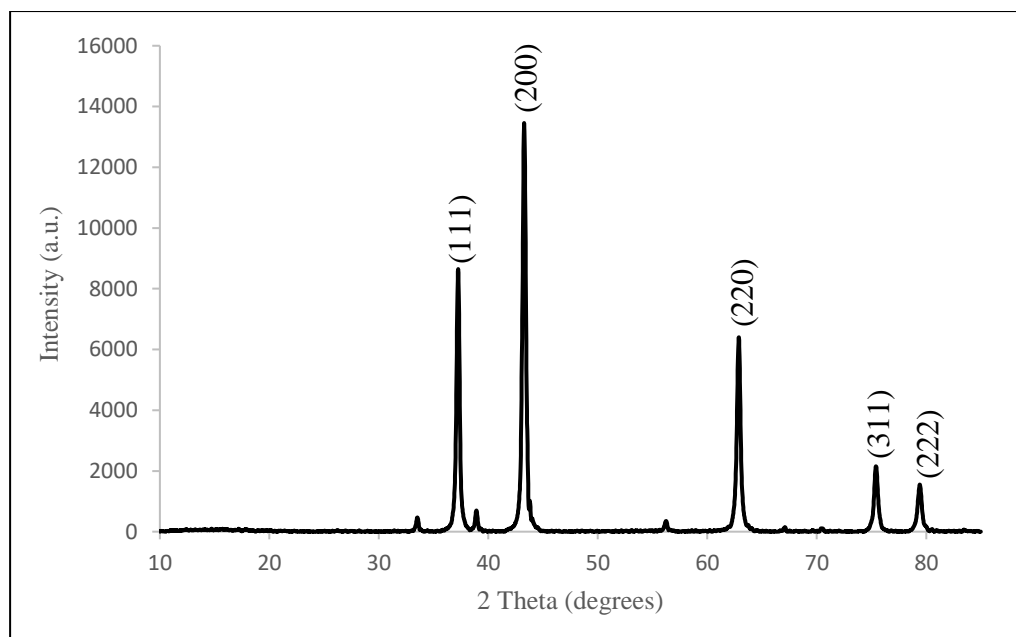


Figure 4.15: XRD diffractogram of the synthesized NiO NPs using Ni-N as precursor salt.

Figure 4.15 presents the XRD diffractogram showing the crystalline structure of NiO nanoparticles synthesized from Ni-N. The diffraction peaks were detected at 2θ angles of 37.27° , 43.31° , 62.91° , 75.36° , and 79.32° , corresponding to the (111), (200), (220), (311), and (222) crystallographic planes respectively. These peaks were 96.9% matched with ICDD Card No. 01-071-4751 as shown in Appendix D. The NiO nanoparticles synthesized exhibited a cubic crystal system with the space group Fm-3m and the calculated lattice parameter was $a = 4.1800 \text{ \AA}$. The crystallinity of the NiO nanoparticles was determined to be 12.63%, with the remaining 87.37% being amorphous content by weight.

The crystallite size for both NiO NPs synthesized by Ni-A and Ni-N for each diffraction peak was calculated utilizing the Debye Scherrer equation as detailed in Appendix B. The calculated crystallite sizes were then tabulated in Tables 4.4. As a result, the average crystallite sizes were found to be 18.53 nm for the NiO NPs synthesized from Ni-A and 27.22 nm for those synthesized from Ni-N.

The difference in the crystal system exhibited by utilizing different precursor salts owing to a slight distortion occurred in the direction (111) (Palanisamy, and Raichur, 2009). It was proven by observing that the diffraction peak at (111) was asymmetric and splitting occurred due to phase transformation from cubic to rhombohedral. This causes the cubic unit cell's body diagonal to either elongate or compress. As the rhombohedral unit cell has two distinct body-diagonal lengths, the (111) cubic reflection separates into two unique peaks. However, the (100) cubic peak maintains the same (Mikhnenko et al., 2023). Additionally, the presence of various anions in different nickel salts influences the nucleation and growth of NiO nanoparticles by creating distinct environments for their formation, which in turn alters the arrangement and surface features of the faceted planes (Abdullah et al., 2024; Chan et al., 2024).

The broad diffraction peaks were observed in Figure 4.14 (rhombohedral structure) suggesting the amorphous character of the synthesized NPs. In contrast, Figure 4.15 (cubic structure) showed sharp and narrow peaks that correspond to the crystallinity of NPs (Abraham et al., 2020). This was well

supported by the higher amorphous content of the rhombohedral structure of NiO NPs (87.59 %) as compared to the cubic structure (87.37%).

Table 4.4: Crystallite size calculated using the Debye-Scherrer's equation using Ni-A and Ni-N as precursor salts.

NiO (Ni-A)					NiO (Ni-N)				
2θ	Miller's index	FWHM (°)	β (radians)	D (nm)	2θ	Miller's index	FWHM (°)	β (radians)	D (nm)
37.27	(111)	0.44	0.00768	19.05	37.27	(111)	0.32	0.00559	26.20
43.32	(200)	0.48	0.00838	17.81	43.31	(200)	0.32	0.00559	26.71
62.84	(220)	0.56	0.00977	16.62	62.91	(220)	0.36	0.00628	25.87
75.4	(311)	0.52	0.00908	19.31	75.36	(311)	0.40	0.00698	25.09
79.34	(222)	0.52	0.00908	19.85	79.32	(222)	0.32	0.00559	32.25

CHAPTER 5

CONCLUSION

5.1 Conclusion

In this project, NiO NPs can be synthesized from the aqueous extract barks of *M. calabura* through a green synthesis pathway using Ni-A and Ni-N as precursor salts. A substantial amount of research has focused on plant extracts while relatively few studies have investigated the optical properties and morphology of NiO nanoparticles made from various precursor salts. Additionally, research on the bark of *M. calabura* is limited as most studies tend to use other plant species. Consequently, this study is considered significant. Next, synthesized NiO NPs were characterized using UV-Vis, FT-IR, SEM, EDX, and XRD.

The synthesized NiO NPs using Ni-A as precursor salt obtained the maximum absorption peak at 346 nm with a band gap energy of 3.58 eV. A significant FTIR band was observed at 479 cm^{-1} corresponding to NiO stretching vibration which indicates the NiO NPs were successfully synthesized. The synthesized NiO NPs were spherical with particle sizes ranging from 44.7 - 65.6 nm. It exhibited a trigonal (hexagonal axes) structure with an average crystallite size of 18.53 nm.

The NiO nanoparticles synthesized from Ni-N as the precursor salt showed a maximum absorption peak at 340 nm and a band gap energy of 3.64 eV. The FTIR band at 460 cm^{-1} were attributed to the NiO stretching vibration and this confirmed the successful synthesis of NiO nanoparticles. Furthermore, the NiO NPs were spherical with sizes ranging from 37.8 - 61.6 nm. It exhibited a cubic structure with an average crystallite size of 27.22 nm.

5.2 Further studies

The yield of NiO NPs produced can be improved by investigating several variables, including temperature, solvent type, plant biomolecules, pH level, extract and salt concentrations, and the duration of the reaction. The characterization of NiO NPs can be further studied by using different precursor salts to determine the variations in the resulting properties. The phytochemical screening tests for the bark of *M. calabura* can be conducted to identify the bioactive compounds that act as reducing, stabilizing, and encapsulating compounds in the production of NiO NPs. Additionally, the synthesized NiO nanoparticles can be further characterized using transmission electron microscopy (TEM) to reveal their detailed internal structure, and Raman spectroscopy to analyze nonpolar bonds and symmetric vibrations. Lastly, synthesized NiO NPs are applicable in numerous fields including the photodegradation of dye, semiconductors, and others owing to their unique characteristics.

References

- Abdullah, J. A. A., Guerrero, A. and Romero, A., 2024. Efficient and sustainable synthesis of zinc salt-dependent polycrystal zinc oxide nanoparticles: Comprehensive assessment of physicochemical and functional properties. *Applied sciences (Basel, Switzerland)*, 14(5), p. 1815. doi: 10.3390/app14051815.
- Abraham, J. *et al.*, 2020. Characterization of green nanoparticles from plants, in *Phytonanotechnology*. Elsevier, pp. 21–39.
- Abubakar, A. and Haque, M., 2020. Preparation of medicinal plants: Basic extraction and fractionation procedures for experimental purposes. *Journal of pharmacy & bioallied sciences*, 12(1), p. 1. doi: 10.4103/jpbs.jpbs_175_19.
- Ahmad, W. *et al.*, 2022. A review on current trends in the green synthesis of nickel oxide nanoparticles, characterizations, and their applications. *Environmental Nanotechnology Monitoring & Management*, 18(100674), p. 100674. doi: 10.1016/j.enmm.2022.100674.
- Alhalili, Z., 2023. Metal oxides nanoparticles: General structural description, chemical, physical, and biological synthesis methods, role in pesticides and heavy metal removal through wastewater treatment. *Molecules (Basel, Switzerland)*, 28(7), p. 3086. doi: 10.3390/molecules28073086.
- Altammar, K. A., 2023. A review on nanoparticles: characteristics, synthesis, applications, and challenges. *Frontiers in microbiology*, 14. doi: 10.3389/fmicb.2023.1155622.
- Aminuzzaman, M. *et al.*, 2021. Biosynthesis of NiO nanoparticles using soursop (*Annona muricata* L.) fruit peel green waste and their photocatalytic performance on crystal Violet dye. *Journal of cluster science*, 32(4), pp. 949–958. doi: 10.1007/s10876-020-01859-8.

Azad, A. *et al.*, 2023. Factors influencing the green synthesis of metallic nanoparticles using plant extracts: A comprehensive review. *Pharmaceutical Fronts*, 05(03). doi:10.1055/s-0043-1774289.

Azadeh, N. A., 2008. *Cognition, Blogspot.com* [Online]. Available at: <https://genuspolitics.blogspot.com/2008/10/doping-of-semiconductors-n-type-and-p.html> [Accessed: August 18, 2024].

Barik, T. K. *et al.*, 2021. Nanomaterials: An Introduction, in *Nanomaterials and Their Biomedical Applications*. Singapore: Springer Singapore, pp. 1–27.

Bastús, N.G., Comenge, J. and Puentes, V., 2011. Kinetically controlled seeded growth synthesis of citrate-stabilized gold nanoparticles of up to 200 nm: Size focusing versus Ostwald ripening. *Langmuir*, 27(17), pp. 11098–11105. doi:10.1021/la201938u.

Bayda, S. *et al.*, 2019. The history of nanoscience and nanotechnology: From chemical–physical applications to nanomedicine. *Molecules (Basel, Switzerland)*, 25(1), p. 112. doi: 10.3390/molecules25010112.

CABI, 2022. *Euphorbia heterophylla* (wild poinsettia), *CABI Compendium*. CABI Publishing.

Chan, Y. B. *et al.*, 2024. *Garcinia mangostana* L. leaf-extract-assisted green synthesis of CuO, ZnO and CuO-ZnO nanomaterials for the photocatalytic degradation of palm oil mill effluent (POME). *Catalysts (Basel, Switzerland)*, 14(8), p. 486. doi: 10.3390/catal14080486.

Chavali, M. S. and Nikolova, M. P., 2019. Metal oxide nanoparticles and their applications in nanotechnology. *SN applied sciences*, 1(6). doi: 10.1007/s42452-019-0592-3.

Diao, C.-C. *et al.*, 2020. Morphological, optical, and electrical properties of p-type nickel oxide thin films by nonvacuum deposition. *Nanomaterials (Basel, Switzerland)*, 10(4), p. 636. doi: 10.3390/nano10040636.

El-Kemary, M., Nagy, N. and El-Mehasseb, I., 2013. Nickel oxide nanoparticles: Synthesis and spectral studies of interactions with glucose. *Materials science in semiconductor processing*, 16(6), pp. 1747–1752. doi: 10.1016/j.mssp.2013.05.018.

Epp, J., 2016. X-ray diffraction (XRD) techniques for materials characterization, in *Materials Characterization Using Nondestructive Evaluation (NDE) Methods*. Elsevier, pp. 81–124.

Gandouzi, M. *et al.*, 2023. DFT study of structural optoelectronic and thermoelectric properties of CuNiO ferromagnetic alloys. *Physica Scripta*, 98(7), pp.075936–075936. doi:<https://doi.org/10.1088/1402-4896/acdd2e>.

García-Pinel, B. *et al.*, 2019. Lipid-based nanoparticles: Application and recent advances in cancer treatment. *Nanomaterials (Basel, Switzerland)*, 9(4), p. 638. doi: 10.3390/nano9040638.

Gordon, S. H. *et al.*, 2010. A chemometric method for correcting Fourier transform infrared spectra of biomaterials for interference from water in KBr discs. *Applied spectroscopy*, 64(4), pp. 448–457. doi: 10.1366/000370210791114301.

Gosens, I. *et al.*, 2010. Impact of agglomeration state of nano- and submicron sized gold particles on pulmonary inflammation. *Particle and fibre toxicology*, 7(1), p. 37. doi: 10.1186/1743-8977-7-37.

Groarke, R. *et al.*, 2021. Powder characterization—methods, standards, and state of the art, in *Fundamentals of Laser Powder Bed Fusion of Metals*. Elsevier, pp. 491–527.

Haider, A. *et al.*, 2020. Green synthesized phytochemically (*Zingiber officinale* and *Allium sativum*) reduced nickel oxide nanoparticles confirmed bactericidal and catalytic potential. *Nanoscale research letters*, 15(1), p. 50. doi: 10.1186/s11671-020-3283-5.

Hano, C. and Abbasi, B. H., 2021. Plant-based green synthesis of nanoparticles: Production, Characterization and Applications. *Biomolecules*, 12(1), p. 31. doi: 10.3390/biom12010031.

Haritha, V. *et al.*, 2022. Biogenic synthesis of nickel oxide nanoparticles using *Averrhoa bilimbi* and investigation of its antibacterial, antidiabetic and cytotoxic properties. *Inorganic chemistry communications*, 144(109930), p. 109930. doi: 10.1016/j.inoche.2022.109930.

Hong, S.-J. *et al.*, 2021. Characterization of nickel oxide nanoparticles synthesized under low temperature. *Micromachines*, 12(10), p. 1168. doi: 10.3390/mi12101168.

Imran Din, M. and Rani, A., 2016. Recent advances in the synthesis and stabilization of nickel and nickel oxide nanoparticles: A green adeptness. *International journal of analytical chemistry*, 2016, pp. 1–14. doi: 10.1155/2016/3512145.

Ingle, P. U. *et al.*, 2023. Emerging role of nanotechnology in precision farming, in *Nanotechnology in Agriculture and Agroecosystems*. Elsevier, pp. 71–91.

Javed, R. *et al.*, 2020. Role of capping agents in the application of nanoparticles in biomedicine and environmental remediation: recent trends and future prospects. *Journal of nanobiotechnology*, 18(1), p. 172. doi: 10.1186/s12951-020-00704-4.

Joudeh, N. and Linke, D., 2022. Nanoparticle classification, physicochemical properties, characterization, and applications: a comprehensive review for biologists. *Journal of nanobiotechnology*, 20(1), p. 262. doi: 10.1186/s12951-022-01477-8.

Kannan, K. *et al.*, 2020. Structural studies of bio-mediated NiO nanoparticles for photocatalytic and antibacterial activities. *Inorganic chemistry communications*, 113(107755), p. 107755. Available at: <https://doi.org/10.1016/j.inoche.2019.107755>.

Kato, Y. and Suzuki, M., 2020. Synthesis of metal nanoparticles by microorganisms. *Crystals*, 10(7), p. 589. doi: 10.3390/cryst10070589.

Kuchekar, M. *et al.*, 2021. *Muntingia calabura*: A comprehensive review. *Journal of Pharmaceutical and Biological Sciences*, 9(2), pp. 81–87. doi: 10.18231/j.jpbs.2021.011.

Lakshmi priya, M. *et al.*, 2017. Nanofiber composites in gene delivery, in *Nanofiber Composites for Biomedical Applications*. Elsevier, pp. 253–274.

Lingaraju, K. *et al.*, 2020. Biosynthesis of Nickel oxide Nanoparticles from *Euphorbia heterophylla* (L.) and their biological application. *Arabian journal of chemistry*, 13(3), pp. 4712–4719. doi: 10.1016/j.arabjc.2019.11.003.

Mahadevaswamy, M. *et al.*, 2022. Plant-mediated synthesis of NiO(II) from *Lantana camara* flowers: a study of photo-catalytic, electrochemical, and biological activities. *Journal of materials research and technology*, 19, pp. 4543–4556. doi: 10.1016/j.jmrt.2022.06.166.

Mahmood, N. D. *et al.*, 2014. *Muntingia calabura*: A review of its traditional uses, chemical properties, and pharmacological observations. *Pharmaceutical biology*, 52(12), pp. 1598–1623. doi: 10.3109/13880209.2014.908397.

Maind, R. *et al.*, 2024. Nickel oxide based nanoparticles: Green synthesis, morphological assessment, and their biological properties. *Universal Journal of Green Chemistry*, pp. 229–254. doi: 10.37256/ujgc.2220244754.

Malik, S., Muhammad, K. and Waheed, Y., 2023. Nanotechnology: A revolution in modern industry. *Molecules (Basel, Switzerland)*, 28(2), p. 661. doi: 10.3390/molecules28020661.

Mallikharjuna, P.B. *et al.*, 2007. Phytochemical studies of *strychnos potatorum* L.F.- a medicinal plant. *Journal of Chemistry*, 4(4), pp. 510–518. doi:10.1155/2007/687859.

Mekuye, B. and Abera, B., 2023. Nanomaterials: An overview of synthesis, classification, characterization, and applications. *Nano select: open access*, 4(8), pp. 486–501. doi: 10.1002/nano.202300038.

Mikhnenko, M. D. *et al.*, 2023. Defect structure of nanocrystalline NiO oxide stabilized by SiO₂. *Inorganics*, 11(3), p. 97. doi: 10.3390/inorganics11030097.

Nasrollahzadeh, M. *et al.*, 2019. Plant-mediated green synthesis of nanostructures: Mechanisms, characterization, and applications, in *Interface Science and Technology*. Elsevier, pp. 199–322.

Nyabadza, A. *et al.*, 2023. A review of physical, chemical and biological synthesis methods of bimetallic nanoparticles and applications in sensing, water treatment, biomedicine, catalysis and hydrogen storage. *Advances in colloid and interface science*, 321(103010), p. 103010. doi: 10.1016/j.cis.2023.103010.

Palanisamy, P. and Raichur, A. M., 2009. Synthesis of spherical NiO nanoparticles through a novel biosurfactant mediated emulsion technique. *Materials science & engineering. C, Materials for biological applications*, 29(1), pp. 199–204. doi: 10.1016/j.msec.2008.06.008.

Pratiwi, E. D. and Dewi, N. P., 2022. Screening of Phytochemical Secondary Metabolites of *Muntingia Calabura*: a Potential as Hepatoprotector. *Journal of Fundamental and Applied Pharmaceutical Science*, 2(2), pp. 59–65. doi: 10.18196/jfaps.v2i2.12364.

Priya, G.T. and Yasmin, Y., 2022. Phytochemicals and Antibacterial Activity of Muntingia calabura Leaves Based Product. *Journal of Research in Medical and Dental Science*, 10(11), pp. 259–263.

Pryshchepa, O., Pomastowski, P. and Buszewski, B., 2020. Silver nanoparticles: Synthesis, investigation techniques, and properties. *Advances in colloid and interface science*, 284(102246), p. 102246. doi: 10.1016/j.cis.2020.102246.

Qamar, S. U. R. and Ahmad, J. N., 2021. Nanoparticles: Mechanism of biosynthesis using plant extracts, bacteria, fungi, and their applications. *Journal of molecular liquids*, 334(116040), p. 116040. doi: 10.1016/j.molliq.2021.116040.

Quevedo, A. C. *et al.*, 2021. UV-Vis spectroscopic characterization of nanomaterials in aqueous media. *Journal of visualized experiments: JoVE*, (176). doi: 10.3791/61764.

Quiroga Ledezma, C. C., 2020. Native food crops for present and future generations, in *Sustainability of the Food System*. Elsevier, pp. 3–23.

Rabouw, F. T. and de Mello Donega, C., 2016. Excited-state dynamics in colloidal semiconductor nanocrystals. *Topics in current chemistry (Journal)*, 374(5). doi: 10.1007/s41061-016-0060-0.

Reis, M., 2013. Long-range ordering, in *Fundamentals of Magnetism*. Elsevier, pp. 147–175.

Ritu *et al.*, 2023. Phytochemical-based synthesis of silver nanoparticle: Mechanism and potential applications. *BioNanoScience*, 13(3), pp. 1359–1380. doi: 10.1007/s12668-023-01125-x.

Sabouri, Z. *et al.*, 2021. Green synthesis of nickel oxide nanoparticles using *Salvia hispanica* L. (chia) seeds extract and studies of their photocatalytic activity and cytotoxicity effects. *Bioprocess and biosystems engineering*, 44(11), pp. 2407–2415. doi: 10.1007/s00449-021-02613-8.

Sagadevan, S. and Podder, J., 2015. Investigations on structural, optical, morphological and electrical properties of nickel oxide nanoparticles. *International journal of nanoparticles*, 8(3/4), p. 289. doi: 10.1504/ijnp.2015.073731.

Selvanathan, V. *et al.*, 2021. *Muntingia calabura* leaves mediated green synthesis of CuO nanorods: Exploiting phytochemicals for unique morphology. *Materials*, 14(21), p. 6379. doi: 10.3390/ma14216379.

Shah, T. R., Babar, H. and Ali, H. M., 2021. Energy harvesting: role of hybrid nanofluids, in *Emerging Nanotechnologies for Renewable Energy*. Elsevier, pp. 173–211.

Shih, C.-D., 2009. Activation of nitric oxide/cGMP/PKG signaling cascade mediates antihypertensive effects of *Muntingia calabura* in anesthetized spontaneously hypertensive rats. *The American Journal of Chinese Medicine*, 37(06), pp. 1045–1058. doi: 10.1142/s0192415x0900748x.

Singh, I., 2023. *Green chemistry, Odebo* [Online]. Available at: <https://odebohome.in/blogs/news/green-chemistry> [Accessed: August 17, 2024].

Uddin, S. *et al.*, 2021. Green synthesis of nickel oxide nanoparticles from *Berberis balochistanica* stem for investigating bioactivities. *Molecules (Basel, Switzerland)*, 26(6), p. 1548. doi: 10.3390/molecules26061548.

Vattuone, L., Savio, L. and Rocca, M., 2018. Influence of defects on adsorption—model studies with stepped surfaces, in *Encyclopedia of Interfacial Chemistry*. Elsevier, pp. 138–165.

Wahid Wahab, A. *et al.*, 2018. Bio-synthesis of gold nanoparticles through bioreduction using the aqueous extract of *Muntingia calabura* L. leaf. *Oriental journal of chemistry*, 34(1), pp. 401–409. doi: 10.13005/ojc/340143.

Wardani, M. *et al.*, 2019. Synthesis of NiO nanoparticles via green route using *Ageratum conyzoides* L. leaf extract and their catalytic activity. *IOP conference series: Materials science and engineering*, 509, p. 012077. Available at: <https://doi.org/10.1088/1757-899x/509/1/012077>.

Yaqoob, A. A. *et al.*, 2020. Recent advances in metal decorated nanomaterials and their various biological applications: A review. *Frontiers in chemistry*, 8. doi: 10.3389/fchem.2020.00341.

Zakaria, Z. A. *et al.*, 2006. The antinociceptive activity of *Muntingia calabura* aqueous extract and the involvement of l-arginine/nitric oxide/cyclic guanosine monophosphate pathway in its observed activity in mice. *Fundamental & clinical pharmacology*, 20(4), pp. 365–372. doi: 10.1111/j.1472-8206.2006.00412.x.

Zakaria, Z. A. *et al.*, 2007. The antinociceptive action of aqueous extract from *Muntingia calabura* leaves: The role of opioid receptors. *Medical principles and practice: international journal of the Kuwait University, Health Science Centre*, 16(2), pp. 130–136. doi: 10.1159/000098366.

Zinn, A. A. *et al.*, 2013. Nanoparticle paste formulations and methods for production and use thereof, *World Patent*.

APPENDICES

Appendix A

Calculation for band gap energy, E_g :

$$\text{Band gap energy, } E_g = \frac{hc}{\lambda}$$

Where,

h = Planck's constant (6.626×10^{-34} Js)

c = Speed of light (3.00×10^8 ms⁻¹)

λ = Maximum absorption wavelength (346 and 340 nm)

Appendix B

Calculation for β for NiO (Ni-A):

$$\begin{aligned}\beta &= \frac{\text{FWHM in } 2\theta \times \pi}{180^\circ} \\ &= \frac{0.44 \times \pi}{180^\circ} \\ &= 7.68 \times 10^{-3} \text{ radians}\end{aligned}$$

Calculation for crystallite size by Debye-Scherrer Equation for NiO (Ni-A):

$$D = \frac{K\lambda}{\beta \cos\theta}$$

Where,

D = Crystallite size in diameter

K = Scherrer constant, 0.9

λ = Wavelength of X-ray source (Cu K α radiation= 1.5406 Å)

β = Full width at half maximum (FWHM) of the diffraction peak in radian 2θ

θ = Bragg's angle of diffraction

$$\begin{aligned}D &= \frac{K\lambda}{\beta \cos\theta} \\ &= \frac{0.9 (1.5406 \times 10^{-10} \text{ m})}{7.68 \times 10^{-3} \text{ radians} (\cos 18.635^\circ)} \\ &= 1.905 \times 10^{-8} \text{ m} \\ &= 19.05 \text{ nm}\end{aligned}$$

A similar calculation was conducted for the remaining matched peaks for NiO NPs (Ni-A and Ni-N) to determine their average crystallite sizes as presented in the tables below:

Tables: Calculation of the average crystallite size.

NiO (Ni-A)				
2 θ	Miller's index	FWHM (°)	β (radians)	D (nm)
37.27	(111)	0.44	0.00768	19.05
43.32	(200)	0.48	0.00838	17.81
62.84	(220)	0.56	0.00977	16.62
75.4	(311)	0.52	0.00908	19.31
79.34	(222)	0.52	0.00908	19.85
Average				18.53

NiO (Ni-N)				
2 θ	Miller's index	FWHM (°)	β (radians)	D (nm)
37.27	(111)	0.32	0.00559	26.20
43.31	(200)	0.32	0.00559	26.71
62.91	(220)	0.36	0.00628	25.87
75.36	(311)	0.40	0.00698	25.09
79.32	(222)	0.32	0.00559	32.25
Average				27.22

Appendix C

```

*** Basic Data Process ***

Group      : Standard
Data      : KWF_NiO_A

# Strongest 3 peaks
no. peak  2Theta      d      I/I1  FWHM      Intensity  Integrated Int
          no.      (deg)    (Å)      (deg)    (Counts)  (Counts)
  1      4      43.2854  2.08857  100  0.48930   8805   240051
  2      1      37.2394  2.41258   61  0.48500   5393   159472
  3      8      62.8846  1.47669   41  0.60930   3622   120552

# Peak Data List
peak      2Theta      d      I/I1  FWHM      Intensity  Integrated Int
no.      (deg)    (Å)      (deg)    (Counts)  (Counts)
  1      37.2394  2.41258   61  0.48500   5393   159472
  2      38.9090  2.31281    5  0.45060    418   13619
  3      42.3800  2.13107    4  0.52360    314   23380
  4      43.2854  2.08857  100  0.48930   8805   240051
  5      44.4727  2.03553   28  0.33490   2486   50013
  6      51.8316  1.76250   10  0.35630    880   17630
  7      62.2600  1.49000    6  0.38360    565   19991
  8      62.8846  1.47669   41  0.60930   3622   120552
  9      75.4228  1.25931   14  0.68880   1226   46976
 10      76.3400  1.24645    6  0.44000    513   14079
 11      79.4031  1.20588   10  0.67950    837   37062

```

Figure: XRD information of synthesized NiO NPs (Ni-A) 96.0 % matching with 96.0 % matched with ICDD Card No. 01-071-6724 (Part I).

```

*** Basic Data Process ***

# Data Information
  Group           : Standard
  Data            : KWF_NiO_A
  Sample Name     : NiO_A
  Comment         :
  Date & Time     : 06-27-24 14:38:38

# Measurement Condition
  X-ray tube
    target        : Cu
    voltage       : 40.0 (kV)
    current       : 30.0 (mA)
  Slits
    Auto Slit     : not Used
    divergence slit : 1.00000 (deg)
    scatter slit  : 1.00000 (deg)
    receiving slit : 0.30000 (mm)
  Scanning
    drive axis    : Theta-2Theta
    scan range    : 10.0000 - 85.0000 (deg)
    scan mode     : Continuous Scan
    scan speed    : 2.0000 (deg/min)
    sampling pitch : 0.0200 (deg)
    preset time   : 0.60 (sec)

# Data Process Condition
  Smoothing [ AUTO ]
    smoothing points : 27
  B.G.Subtraction [ AUTO ]
    sampling points : 29
    repeat times   : 30
  Kal-a2 Separate [ MANUAL ]
    Kal a2 ratio   : 50 (%)
  Peak Search [ AUTO ]
    differential points : 25
    FWHM threshold   : 0.050 (deg)
    intensity threshold : 30 (par mil)
    FWHM ratio (n-1)/n : 2
  System error Correction [ NO ]
  Precise peak Correction [ NO ]

```

Figure: XRD information of synthesized NiO NPs (Ni-A) 96.0 % matching with 96.0 % matched with ICDD Card No. 01-071-6724 (Part II).

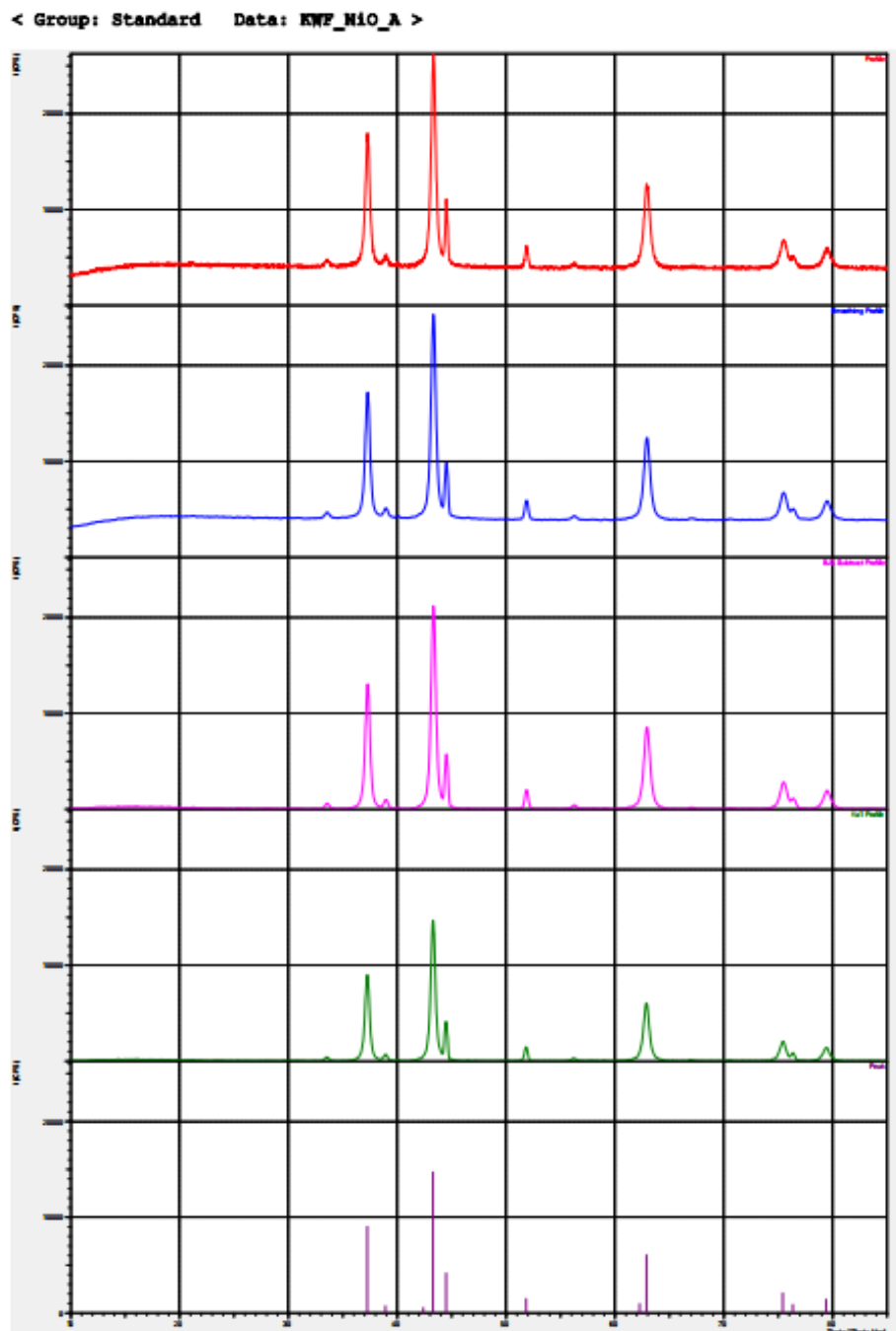


Figure: XRD information of synthesized NiO NPs (Ni-A) 96.0 % matching with 96.0 % matched with ICDD Card No. 01-071-6724 (Part III).

Match! Phase Analysis Report

Universiti Tunku Abdul Rahman, Faculty of Science

Sample: NiO_A ()

Sample Data

File name KWF_NiO_A.RAW
File path C:/xdat/Standard/KWF_NiO_A
Data collected Jun 27, 2024 15:18:02
Data range 10.000° - 85.000°
Original data range 10.000° - 85.000°
Number of points 3751
Step size 0.020
Rietveld refinement converged No
Alpha2 subtracted No
Background subtr. No
Data smoothed No
Radiation X-rays
Wavelength 1.540600 Å

Matched Phases

Index	Amount (%)	Name	Formula sum
A	96.0	Nickel Oxide	Ni O
	4.0	Unidentified peak area	

A: Nickel Oxide (96.0 %)

Formula sum Ni O
Entry number 01-071-6724
Figure-of-Merit (FoM) 0.930467
Total number of peaks 18
Peaks in range 18
Peaks matched 9
Intensity scale factor 0.64
Space group R-3m
Crystal system trigonal (hexagonal axes)
Unit cell a= 2.9549 Å c= 7.2320 Å
V/c 4.74
Calc. density 6.805 g/cm³
Reference Rodic, D., Spasojevic, V., Kusigerski, V., Tellgren, R., Rundlof, H. Rodic, D., Spasojevic, V., Kusigerski, V., Tellgren, R., Rundlof, H., Golden Book of Phase Transitions, Wroclaw **1218**, 1527 (20022000)

Candidates

Name	Formula	Entry No.	FoM
Ethylenediammonium hexaaquanickel bis(sulfate)	C2 H22 N2 Ni O14 S2	00-058-1847	0.7670
Potassium Nickel Fluoride Hydrate	K Ni F3 H2 O	00-045-0225	0.7481
Nickel Iodate	Ni (I O3)2	00-033-0946	0.6822
Lanthanum Strontium Nickel Oxide	(La Sr) Ni O3.43	01-081-0825	0.6324
Strontium Barium Nickel Manganese Oxide	(Sr0.75 Ba0.25)5 (Ni Mn3 O12)	01-072-8239	0.6231
Nickel Ammine Nitrate	Ni (N O3)2 (N H3)6	00-045-0027	0.6159
Neodymium Strontium Nickel Copper Oxide	Nd Sr Ni0.8 Cu0.2 O3.94	01-075-3671	0.6015

Search-Match

Settings
Reference database used PDF-2 Release 2016 RDB
Automatic zeropoint adaptation Yes
Minimum figure-of-merit (FoM) 0.60
2theta window for peak corr. 0.30 deg.
Minimum rel. int. for peak corr. 1
Parameter/influence 2theta 0.50
Parameter/influence intensities 0.50
Parameter multiple/single phase(s) 0.50

Figure: XRD information of synthesized NiO NPs (Ni-A) 96.0 % matching with 96.0 % matched with ICDD Card No. 01-071-6724 (Part IV).

Selection Criteria

Elements:

Elements that must be present: O, Ni
Elements that may be present: All elements not mentioned above

Peak List

No.	2theta [°]	d [Å]	h/k/l	FWHM	Matched
1	33.51	2.6721	26.30	0.3200	
2	37.27	2.4105	607.13	0.4400	A
3	38.96	2.3101	39.01	0.2800	
4	43.32	2.0868	1000.00	0.4800	A
5	44.51	2.0341	296.18	0.2400	
6	51.87	1.7613	103.09	0.3200	
7	62.84	1.4776	361.02	0.5600	A
8	75.40	1.2596	117.97	0.5200	A
9	76.41	1.2455	46.44	0.3200	
10	79.34	1.2067	72.16	0.5200	A

Rietveld Refinement using FullProf

Calculation was not run or did not converge.

Crystallite Size Estimation using Scherrer Formula

Calculation was not run.

Degree of crystallinity analysis

Profile area	Counts	Amount
Total area	10120142	100.00%
Diffraction peaks	1145369	11.32%
Background	8974773	88.68%
Instrumental background	892103	8.82%
Amorphous phases	8082670	79.87%

Degree of crystallinity (DOC) = 12.41%
Amorphous content (weight %) = 87.59%

Figure: XRD information of synthesized NiO NPs (Ni-A) 96.0 % matching with 96.0 % matched with ICDD Card No. 01-071-6724 (Part V).

Integrated Profile Areas

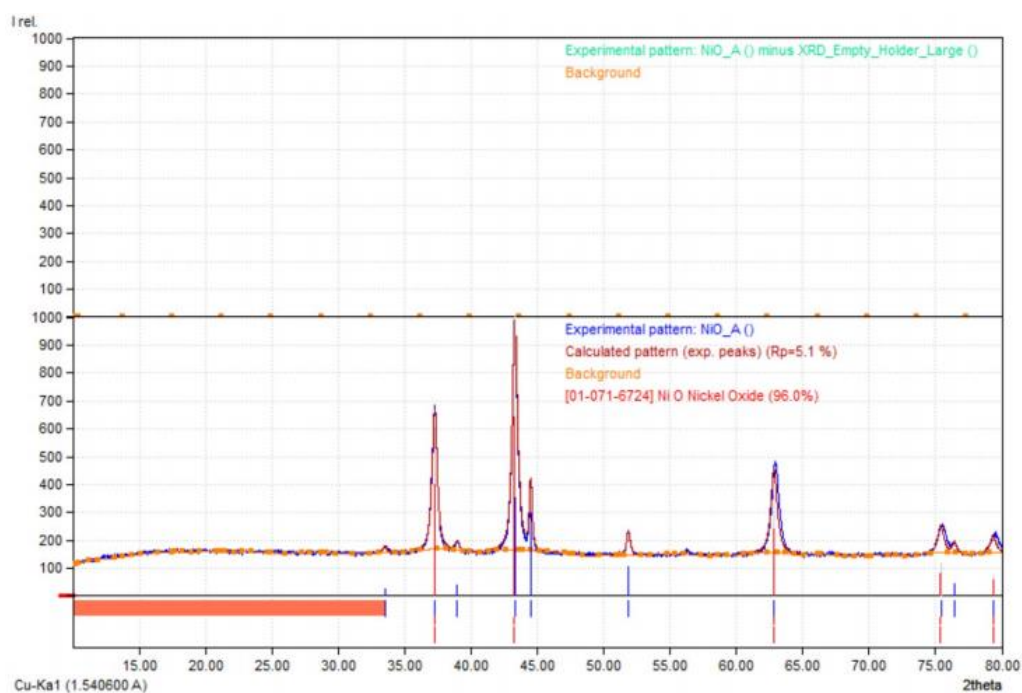
Based on calculated profile

Profile area	Counts	Amount
Overall diffraction profile	10120142	100.00%
Background radiation	8974773	88.68%
Diffraction peaks	1145369	11.32%
Peak area belonging to selected phases	744809	7.36%
Peak area of phase A (Nickel Oxide)	744809	7.36%
Unidentified peak area	400560	3.96%

Peak Residuals

Peak data	Counts	Amount
Overall peak intensity	20270	100.00%
Peak intensity belonging to selected phases	16949	83.62%
Unidentified peak intensity	3321	16.38%

Diffraction Pattern Graphics



PDF Database Copyright International Centre for Diffraction Data (ICDD)
Match! Copyright © 2003-2018 CRYSTAL IMPACT, Bonn, Germany

Figure: XRD information of synthesized NiO NPs (Ni-A) 96.0 % matching with 96.0 % matched with ICDD Card No. 01-071-6724 (Part VI).

Appendix D

```

*** Basic Data Process ***

Group      : Standard
Data       : KWF_NiO_N

# Strongest 3 peaks
no. peak  2Theta      d      I/I1  FWHM      Intensity  Integrated Int
no.      (deg)      (Å)      I/I1  (deg)      (Counts)  (Counts)
  1      4      43.2714   2.08921 100   0.35990   13455   281091
  2      2      37.2348   2.41286  64   0.32180    8647   173707
  3      6      62.8695   1.47701  48   0.37130    6402   150988

# Peak Data List
peak      2Theta      d      I/I1  FWHM      Intensity  Integrated Int
no.      (deg)      (Å)      I/I1  (deg)      (Counts)  (Counts)
  1      33.5170   2.67151   3     0.27160     469      8181
  2      37.2348   2.41286  64     0.32180    8647    173707
  3      38.9080   2.31287   5     0.27330     698     13287
  4      43.2714   2.08921 100     0.35990   13455    281091
  5      43.8400   2.06342   6     0.14900     811     13923
  6      62.8695   1.47701  48     0.37130    6402    150988
  7      75.4119   1.25946  16     0.39900    2148    54525
  8      79.4036   1.20587  11     0.42730    1547     41876

```

Figure: XRD information of synthesized NiO NPs (Ni-N) 96.9% matched with ICDD Card No. 01-071-4751 (Part I).

```

*** Basic Data Process ***

# Data Infomation
  Group           : Standard
  Data            : KWF_NiO_N
  Sample Nmae    : NiO_N
  Comment         :
  Date & Time    : 06-27-24 15:19:34

# Measurement Condition
  X-ray tube
    target        : Cu
    voltage       : 40.0 (kV)
    current       : 30.0 (mA)
  Slits
    Auto Slit    : not Used
    divergenc slit : 1.00000 (deg)
    scatter slit  : 1.00000 (deg)
    receiving slit : 0.30000 (mm)
  Scanning
    drive axis   : Theta-2Theta
    scan range   : 10.0000 - 85.0000 (deg)
    scan mode    : Continuous Scan
    scan speed   : 2.0000 (deg/min)
    sampling pitch : 0.0200 (deg)
    preset time  : 0.60 (sec)

# Data Process Condition
  Smoothing [ AUTO ]
    smoothing points : 19
  B.G.Subtruction [ AUTO ]
    sampling points : 21
    repeat times : 30
  Kal-a2 Separate [ MANUAL ]
    Kal a2 ratio : 50 (%)
  Peak Search [ AUTO ]
    differential points : 19
    FWHM threshold : 0.050 (deg)
    intensity threshold : 30 (par mil)
    FWHM ratio (n-1)/n : 2
  System error Correction [ NO ]
  Precise peak Correction [ NO ]

```

Figure: XRD information of synthesized NiO NPs (Ni-N) 96.9% matched with ICDD Card No. 01-071-4751 (Part II).

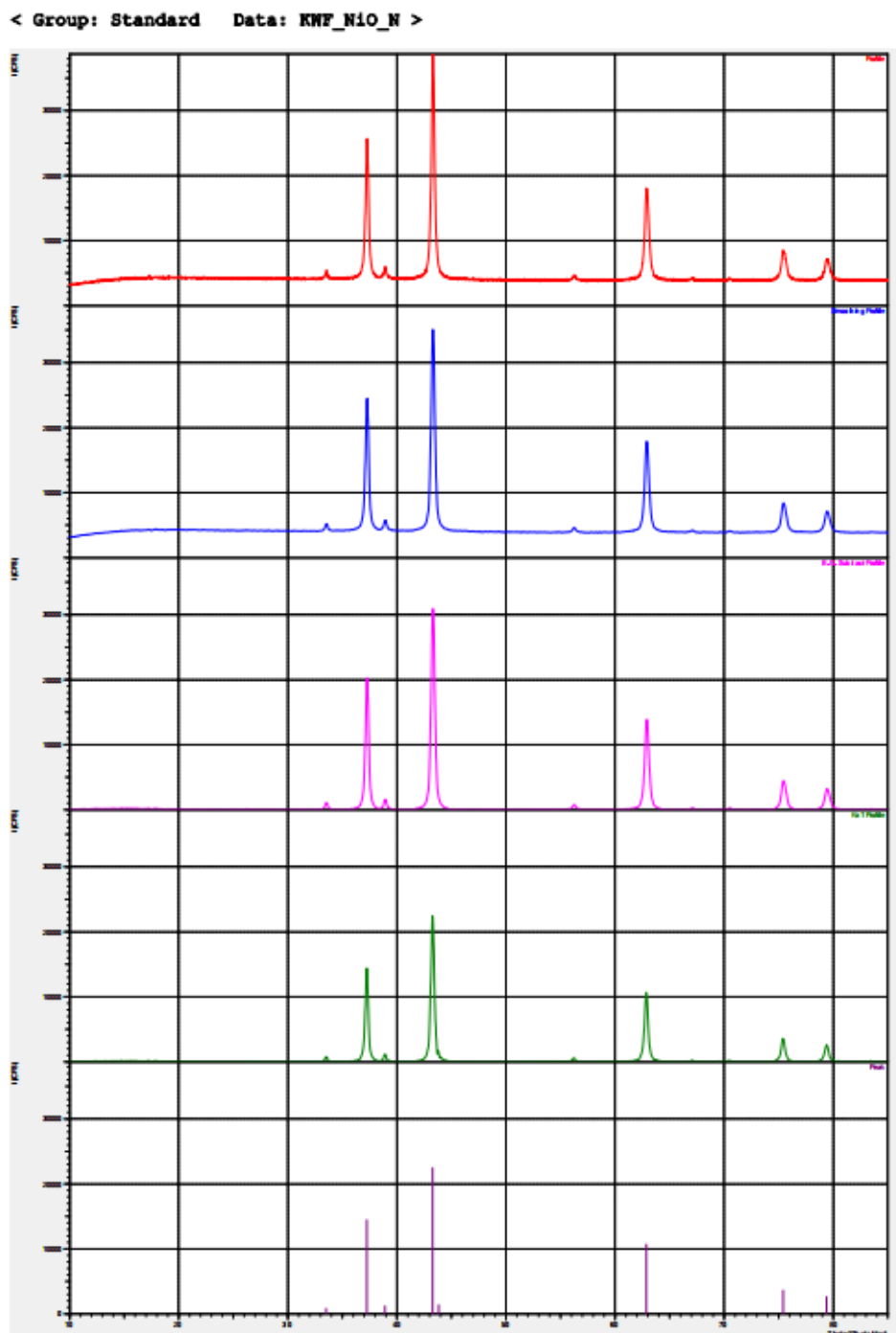


Figure: XRD information of synthesized NiO NPs (Ni-N) 96.9% matched with ICDD Card No. 01-071-4751 (Part III).

Match! Phase Analysis Report

Universiti Tunku Abdul Rahman, Faculty of Science

Sample: NiO_N ()

Sample Data
File name KWF_NiO_N.RAW
File path C:/xdata/Standard/KWF_NiO_N
Data collected Jun 27, 2024 15:59:00
Data range 10.000° - 85.000°
Original data range 10.000° - 85.000°
Number of points 3751
Step size 0.020
Rietveld refinement converged No
Alpha2 subtracted No
Background subtr. No
Data smoothed No
Radiation X-rays
Wavelength 1.540600 Å

Matched Phases

Index	Amount (%)	Name	Formula sum
A	96.9	Nickel Oxide Bunsenite, syn	Ni O
	3.1	Unidentified peak area	

A: Nickel Oxide Bunsenite, syn (96.9 %)

Formula sum Ni O
Entry number 01-071-4751
Figure-of-Merit (FoM) 0.943194
Total number of peaks 10
Peaks in range 10
Peaks matched 5
Intensity scale factor 0.98
Space group Fm-3m
Crystal system cubic
Unit cell a= 4.1800 Å
V/c 4.74
Calc. density 6.794 g/cm³
Reference Brentano, J., Hoffmann, E.O. Brentano, J., Hoffmann, E.O. Brentano, J., Hoffmann, E.O. Brentano, J., Hoffmann, E.O. Brentano, J., Hoffmann, E.O., Golden Book of Phase Transitions, Wroclaw **1243371927**, 16114111847 (20021926192719251927)

Candidates

Name	Formula	Entry No.	FoM
Potassium Nickel Fluoride Hydrate	K Ni F3 H2 O	00-045-0225	0.6628
Nickel iodate	Ni (IO3)2	00-033-0946	0.6481

Search-Match

Settings
Reference database used PDF-2 Release 2016 RDB
Automatic zeropoint adaptation Yes
Minimum figure-of-merit (FoM) 0.60
2theta window for peak corr. 0.30 deg.
Minimum rel. int. for peak corr. 1
Parameter/influence 2theta 0.50
Parameter/influence intensities 0.50
Parameter multiple/single phase(s) 0.50

Figure: XRD information of synthesized NiO NPs (Ni-N) 96.9% matched with ICDD Card No. 01-071-4751 (Part IV).

Selection Criteria

Elements:

Elements that must be present: O, Ni

Elements that may be present: All elements not mentioned above

Peak List

No.	2theta [°]	d [Å]	I/I0	FWHM	Matched
1	33.56	2.6683	32.47	0.1600	
2	37.27	2.4108	616.44	0.3200	A
3	38.88	2.3145	39.69	0.2000	
4	43.31	2.0874	1000.00	0.3200	A
5	56.23	1.6346	20.62	0.2400	
6	62.91	1.4761	408.44	0.3600	A
7	75.36	1.2602	116.82	0.4000	A
8	79.32	1.2069	76.80	0.3200	A

Rietveld Refinement using FullProf

Calculation was not run or did not converge.

Crystallite Size Estimation using Scherrer Formula

Calculation was not run.

Degree of crystallinity analysis

Profile area	Counts	Amount
Total area	10172552	100.00%
Diffraction peaks	1172514	11.53%
Background	9000038	88.47%
Instrumental background	892103	8.77%
Amorphous phases	8107934	79.70%

Degree of crystallinity (DOC) = 12.63%

Amorphous content (weight %) = 87.37%

Figure: XRD information of synthesized NiO NPs (Ni-N) 96.9% matched with ICDD Card No. 01-071-4751 (Part V).

Integrated Profile Areas

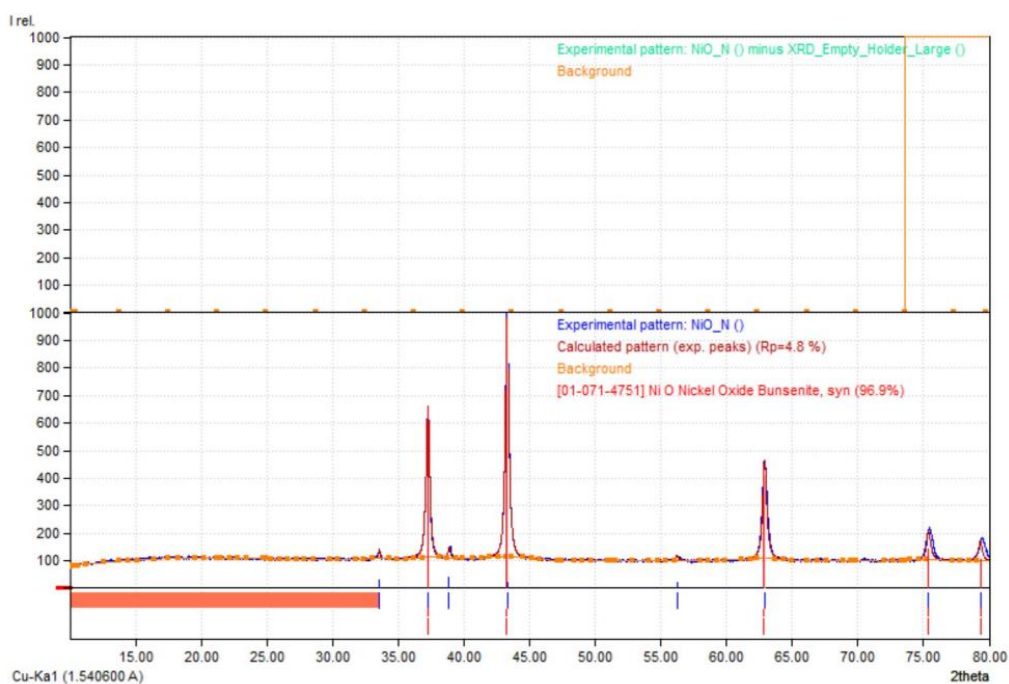
Based on calculated profile

Profile area	Counts	Amount
Overall diffraction profile	10172552	100.00%
Background radiation	9000038	88.47%
Diffraction peaks	1172514	11.53%
Peak area belonging to selected phases	860307	8.46%
Peak area of phase A (Nickel Oxide Bunsenite, syn)	860307	8.46%
Unidentified peak area	312207	3.07%

Peak Residuals

Peak data	Counts	Amount
Overall peak intensity	20055	100.00%
Peak intensity belonging to selected phases	19769	98.57%
Unidentified peak intensity	286	1.43%

Diffraction Pattern Graphics



PDF Database Copyright International Centre for Diffraction Data (ICDD)
Match! Copyright © 2003-2018 CRYSTAL IMPACT, Bonn, Germany

Figure: XRD information of synthesized NiO NPs (Ni-N) 96.9% matched with ICDD Card No. 01-071-4751 (Part VI).